ACS APPLIED MATERIALS & INTERFACES

www.acsami.org

Research Article

# Toolbox of Advanced Atomic Layer Deposition Processes for Tailoring Large-Area $MoS_2$ Thin Films at 150 °C

Miika Mattinen, Jeff J. P. M. Schulpen, Rebecca A. Dawley, Farzan Gity, Marcel A. Verheijen, Wilhelmus M. M. Kessels, and Ageeth A. Bol*

Cite This: *ACS Appl. Mater. Interfaces* 2023, 15, 35565−35579

Read Online

ACCESS | Metrics & More | Article Recommendations | Supporting Information

**ABSTRACT:** Two-dimensional $MoS_2$ is a promising material for applications, including electronics and electrocatalysis. However, scalable methods capable of depositing $MoS_2$ at low temperatures are scarce. Herein, we present a toolbox of advanced plasma-enhanced atomic layer deposition (ALD) processes, producing wafer-scale polycrystalline $MoS_2$ films of accurately controlled thickness. Our ALD processes are based on two individually controlled plasma exposures, one optimized for deposition and the other for modification. In this way, film properties can be tailored toward different applications at a very low deposition temperature of 150 °C. For the modification step, either $H_2$ or Ar plasma can be used to combat excess sulfur incorporation and crystallize the films. Using $H_2$ plasma, a higher degree of crystallinity compared with other reported low-temperature processes is achieved. Applying $H_2$ plasma steps periodically instead of every ALD cycle allows for control of the morphology and enables deposition of smooth, polycrystalline $MoS_2$ films. Using an Ar plasma instead, more disordered $MoS_2$ films are deposited, which show promise for the electrochemical hydrogen evolution reaction. For electronics, our processes enable control of the carrier density from $6 \times 10^{16}$ to $2 \times 10^{21}$ $cm^{-3}$ with Hall mobilities up to 0.3 $cm^2$ $V^{-1}$ $s^{-1}$. The process toolbox forms a basis for rational design of low-temperature transition metal dichalcogenide deposition processes compatible with a range of substrates and applications.

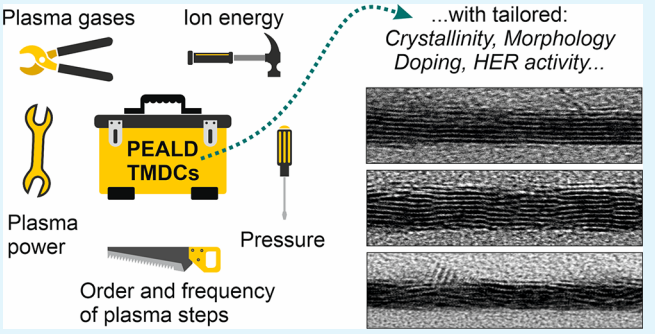


**KEYWORDS:** *2D materials, atomic layer deposition, electrocatalysis, electronics, low-temperature processing, $MoS_2$*

## 1. INTRODUCTION

Two-dimensional (2D) materials rank high among the most scientifically and technologically interesting materials of the early 21st century. Among them, the large family of transition metal dichalcogenides (TMDCs) that includes semiconductors, (semi)metals, and even superconductors[1,2] has drawn intense attention. Besides stability as single, subnanometer thick monolayers, their extraordinary electronic, optical, mechanical, and chemical properties give TMDCs great potential in a range of applications including (opto)electronics, energy storage, and catalysis.[3−5] Some 30 different 2D TMDC materials are known that share the composition $MX_2$, where M is a transition metal or Sn and X is S, Se, or Te. The majority of studies have focused on semiconducting TMDCs, such as $MoS_2$ and $WS_2$, which are among the most promising alternatives to silicon for future nano(opto)electronics.[6−9] The flexible nature of 2D materials also makes them promising for flexible devices including displays and various sensors.[10,11] TMDCs have also been intensively studied for the electrocatalytic hydrogen evolution reaction, a key process in the production of clean hydrogen, where it promises an affordable and sustainable alternative to currently used, scarce Pt.[12−16] Hydrogen is expected to play a major role in the carbon-neutral future, offering a clean, highly efficient fuel, means for grid stabilization, as well as a green alternative for carbon in steel production, for example.[17]

One of the major factors hindering applications of TMDCs in nanoelectronics, electrocatalysis, and other fields alike is the lack of scalable fabrication methods.[5,18] In general, continuous, high-quality films with a controlled and uniform thickness over large, sometimes 3D structured substrates are called for. Many substrates and process flows also place limitations on the applicable thermal budget. Initially, 2D monolayers were produced by mechanical exfoliation of bulk crystals.[19] Although this method remains in use in research for its simplicity and ability to produce high-quality flakes, it cannot be scaled up for production. Chemical vapor deposition (CVD) has emerged as a widespread method for the preparation of high-quality TMDC flakes and films. Its most

Received: February 21, 2023
Accepted: July 4, 2023
Published: July 17, 2023

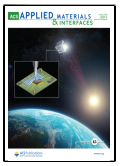

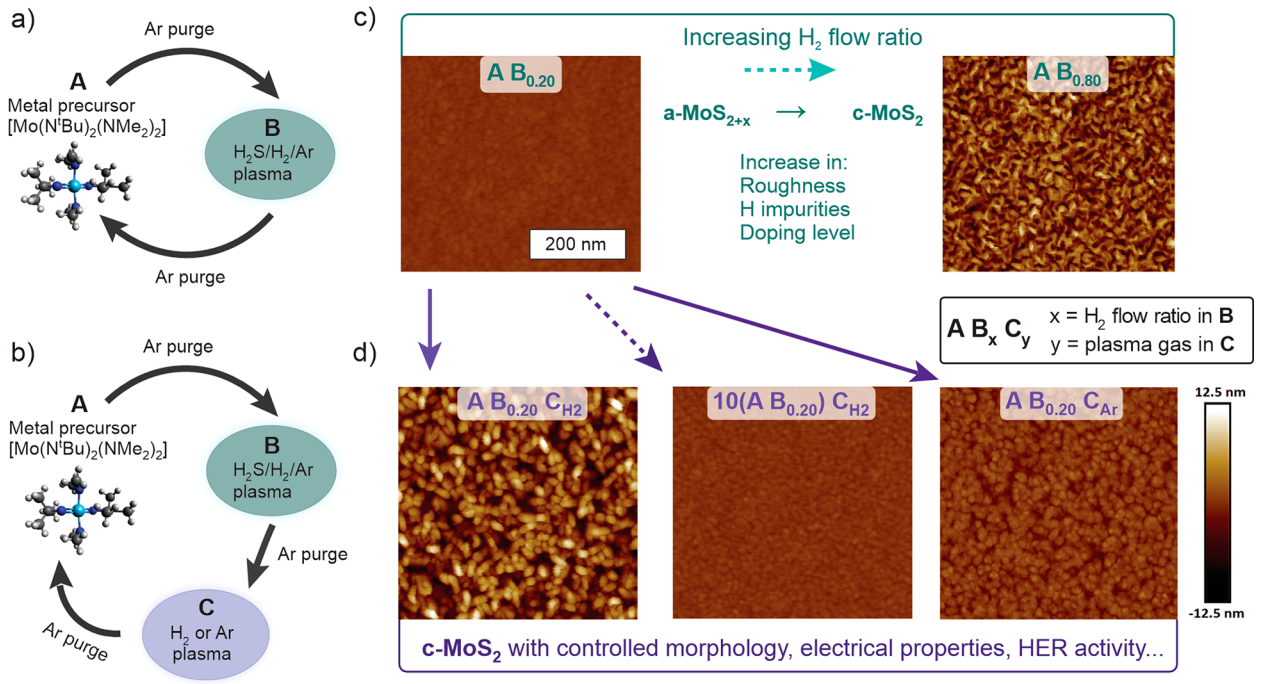


**Figure 1.** Schematic of (a) AB and (b) ABC type PEALD processes and illustration of how the (c) AB and (d) ABC processes enable tailoring of film properties including crystallinity (c = crystalline, a = amorphous) and morphology (atomic force microscopy, AFM, images).

common variant utilizing chalcogenide and metal oxide powder precursors[2,20−22] struggles with thickness control and uniformity and requires high temperatures from 600 to 1000 °C. Use of metalorganic and halide metal precursors and gaseous chalcogenide sources improves scalability and enables a decrease of the deposition temperature to 400−550 °C,[23−25] in favorable cases even 200−300 °C.[26,27] These processes are compatible with back-end-of-line semiconductor processing ($T_{max}$ ≈ 400−500 °C),[28] but cannot be applied on typical plastics and other sensitive materials used in the emerging field of flexible electronics ($T_{max}$ ≈ 100−200 °C). Low processing temperatures also simplify deposition equipment design and require less energy input, which is attractive from both economic and environmental points of view.

Atomic layer deposition (ALD) is an advanced, surface-controlled variant of CVD that boasts excellent uniformity on large areas and complex shapes, accurate thickness control, and high reproducibility and scalability.[29,30] Recently, ALD has been increasingly studied for deposition of TMDCs for a variety of applications.[31,32] ALD processes operate at relatively low temperatures, generally below 500 °C. This is particularly true for its plasma enhanced variant (PEALD) that takes advantage of highly reactive radicals and low-energy ions.[33−35] PEALD processes depositing semiconductors $MoS_2$ and $WS_2$ at 300−450 °C have been developed in our group,[36,37] while metallic $TiS_2$ films could be deposited even at 150 °C.[38]

Recently, we showed that tailoring the plasma deposition chemistry enables a decrease of deposition temperature of both semiconducting and metallic TMDCs to record low 100 °C.[39] The deposition of stoichiometric and crystalline $MoS_2$, $TiS_2$, and $WS_2$ films was achieved by addition of sufficient hydrogen to the $H_2S$ plasma feed gas, which prevents excess S incorporation from otherwise happening at these low temperatures. However, tailoring the chemistry of a single plasma step in such a manner offers limited control over film properties, as the plasma species play multiple simultaneous roles including removal of ligands of the metal precursor, deposition of sulfur, and supplying energy in the form of low-energy ions and other reactive species for creation and healing of defects.

In this study, we show that improved control over film growth and resulting properties can be achieved by using two separate and individually optimized plasma steps. While the first plasma step removes ligands of the metal precursor and supplies sulfur, the second step can be further tailored to control stoichiometry, crystallinity, and electrical properties, among others. We have developed three processes utilizing $H_2$ and Ar plasma steps that deposit uniform, crystalline $MoS_2$ films of accurately controlled thickness at a very low temperature of 150 °C. We discuss the growth mechanisms as well as effect of plasma conditions for each process. Compared to earlier (PE)ALD processes, the new processes exhibit complementary and in many cases improved properties as shown by systematic use of a broad range of microscopy, structural, compositional, and electrical characterization techniques. For electronics, carrier densities can be decreased by 3−5 orders of magnitude, and Hall mobilities increased by an order of magnitude compared to our earlier low-temperature process. For electrocatalytic HER, the catalytic activity can be tailored via changes in the film morphology and crystallinity using the process toolbox developed in this work.

## 2. RESULTS AND DISCUSSION

**2.1. Concept of Developed PEALD Processes.** In this contribution, we explore the ample opportunities that PEALD offers for tailoring TMDC film growth and properties via rational process design and control of process conditions. A typical PEALD process illustrated in Figure 1a begins by exposing a substrate to a metal precursor (denoted A step), in our case a metalorganic Mo precursor $Mo(N^tBu)_2(NMe_2)_2$, which reacts on the substrate surface in self-limiting manner. Then, excess unreacted precursor and byproducts are purged away with the help of Ar gas. The following B step consists of


https://doi.org/10.1021/acsami.3c02466
ACS Appl. Mater. Interfaces 2023, 15, 35565−35579

exposure to a plasma, here a mixed $H_2S/H_2/Ar$ plasma, which removes the ligands of the adsorbed Mo precursor and supplies S, again in a self-limiting manner. A second purge completes an "AB" ALD cycle, which can then be repeated until the target thickness is reached. In such an AB cycle, the plasma conditions of the B step can be varied to tailor film growth and properties. An example of this from our earlier work is shown Figure 1c, illustrating how increasing $H_2$ flow ratio (eq 1) from 0.20 to 0.80 at 150 °C changes the resulting film from amorphous $MoS_{3.5}$ to crystalline $MoS_2$.[39] However, the increase in the $H_2$ flow ratio also leads to incorporation of H dopants into the films, resulting in high carrier densities, a drawback for many semiconductor applications. In addition, high $H_2$ flow ratios, which we denote as a subscript of B (e.g., $B_{0.80}$) lead to rough morphology (Figure 1c). Using intermediate $H_2$ flow ratios (e.g., $B_{0.65}$) results in lower roughness and H impurities, but also poorer crystallinity and electrical properties.[39] These examples illustrate limitations of the AB approach.

$$H_2 \text{ flow ratio} = \frac{H_2 \text{ flow (sccm)}}{H_2 \text{ flow (sccm)} + H_2S \text{ flow (sccm)}} \quad (1)$$

In the "ABC" approach pursued in this work (Figure 1b), we use two separate plasma steps, which allow for more effective decoupling of different atomistic processes and therefore enhanced control over growth and properties of $MoS_x$ films. The first plasma step (B step) is optimized for *deposition*, namely, removing ligands of the adsorbed metal precursor and sulfur deposition. Here, we typically use a low $H_2$ flow ratio in the B step ($B_{0.20}$) to limit H incorporation into the films. The second plasma step (C step) is then used for *modification*, that is, removal of excess S (if present), modifying crystallinity, and tuning film properties. The plasma feed gas in this step is denoted as a subscript of C (e.g., $C_{Ar}$). Thus, we refer to our process with an Ar plasma modification step, for example, as the A $B_{0.20}$ $C_{Ar}$ process.

We have used three different approaches to control the C step: (1) using different plasma gases ($H_2$, Ar, $H_2$/Ar, and $H_2S$/Ar), (2) modifying plasma conditions (such as exposure time, pressure, and plasma power), and (3) changing the frequency or periodicity of the C step, i.e., only applying it every *n* ALD cycles (denoted $n$(A $B_x$) $C_y$). Furthermore, each C step can be combined with different plasma compositions and parameters in the B step, different deposition temperatures, and so forth, giving rise to near infinite possibilities as well as conditions to investigate.

Figure 1d illustrates three optimized processes that can be used to deposit c-$MoS_2$ films of varying stoichiometries, crystallinities, morphologies, and electrical properties. In these processes that form the core of our "toolbox", an A $B_{0.20}$ cycle depositing $MoS_{3.5}$ films was combined with an $H_2$ plasma step either every cycle (A $B_{0.20}$ $C_{H2}$) or every 10 cycles (10(A $B_{0.20}$) $C_{H2}$)) or an Ar plasma step in each cycle (A $B_{0.20}$ $C_{Ar}$) to remove the excess S and crystallize the films. A schematic of the ALD processes is shown in Figure S1 (Supporting Information). Throughout the manuscript, we discuss processes depositing $MoS_2$ at a fixed temperature of 150 °C. The concepts are regardless applicable to other low temperatures, as we show for the A $B_{0.20}$ $C_{H2}$ process, as well as other TMDCs.

These ABC processes allow for submonolayer level thickness control by simply changing the number of ALD cycles (Figure S2 in the Supporting Information) and result in excellent wafer scale uniformity (~2% thickness standard deviation over a 4 in. wafer, Figure S3).

In Section 2.2, we discuss the optimization and mechanisms of these processes. Other explored ABC processes, including those of A $B_{0.80}$ $C_y$ type where the C step is used to modify an already crystalline $MoS_2$ film, are described in the Supporting Information (Section S5). In Section 2.3, we compare the characteristics of films deposited by using the different ABC processes. Finally, in Section 2.4, we explore the application of our $MoS_2$ films as HER catalysts.

**2.2. Characteristics and Optimization of Three ABC Processes.** *2.2.1. Using $H_2$ Plasma: A $B_{0.20}$ $C_{H2}$ process.* The idea of using $H_2$ plasma in a C step builds on our earlier finding of hydrogen preventing excess sulfur incorporation, which otherwise occurs during low-temperature PEALD of TMDCs.[39] Using $H_2S$ plasma with a low $H_2$ flow ratio such as 0.20 yields a-$MoS_{3.5}$ films at 150 °C. In contrast, the A $B_{0.20}$ $C_{H2}$ process results in crystalline c-$MoS_{1.9}$ films at 150 °C as shown by the characteristic $E^1_{2g}$ and $A_{1g}$ Raman modes of $MoS_2$ and stoichiometries determined by XPS (Figure 2). This shows that separate $H_2$ plasma exposure efficiently removes the excess sulfur present in a-$MoS_{3.5}$ and allows for the resulting $MoS_2$ to crystallize. Along with the removal of excess S, the resistivity of the films decreased from >4000 to 3−13 Ω cm and the growth per cycle (GPC) increased from 0.65 to 1.0−1.2 Å. The process showed self-limiting characteristics as expected for ALD in terms of the GPC, S/Mo ratio, resistivity, and Raman intensity (Figure 2 and Section S2.1 in the Supporting Information). A 20 s $H_2$ plasma exposure was deemed saturating and was chosen for further experiments. Besides the temperature of 150 °C discussed here, we found that the process deposited crystalline $MoS_2$ films at temperatures ranging from 100 to 250 °C (Section S2.2 in the Supporting Information).

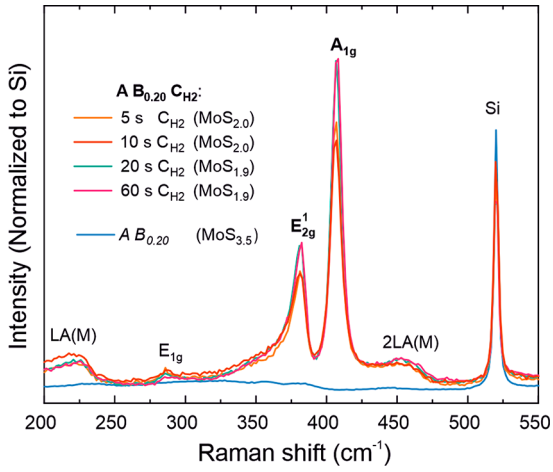


**Figure 2.** Raman spectra and XPS-derived stoichiometries showing the efficient and self-limiting character of the $H_2$ plasma C step in the deposition of c-$MoS_2$ films. The main Raman modes of $MoS_2$ are shown in bold and defect-related and Si modes in normal type (for clarity, LO, TO, and ZO modes are not indicated). The films were deposited by using 140 ALD cycles at 150 °C.

Using $H_2$ gas instead of $H_2$ plasma had no effect on the stoichiometry or crystallinity of a-$MoS_{3.5}$, showing that plasma-generated species such as radicals and ions are essential to the process (Table S1). Using $H_2$ plasma, the crystallinity was


https://doi.org/10.1021/acsami.3c02466
ACS Appl. Mater. Interfaces 2023, 15, 35565−35579

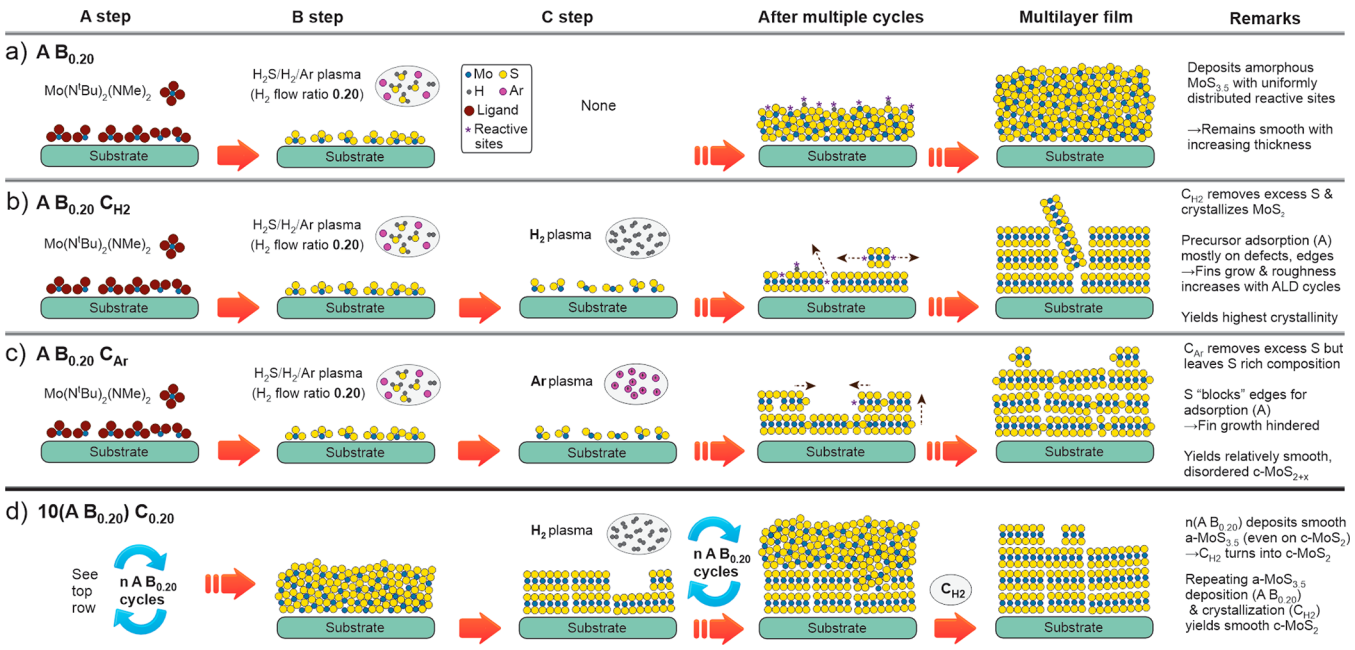


**Figure 3.** Schematic illustration of the (crystal) growth mechanisms and their implications to morphology and microstructure for (a) the reference A $B_{0.20}$ process and (b–d) the three ABC processes developed in this work.

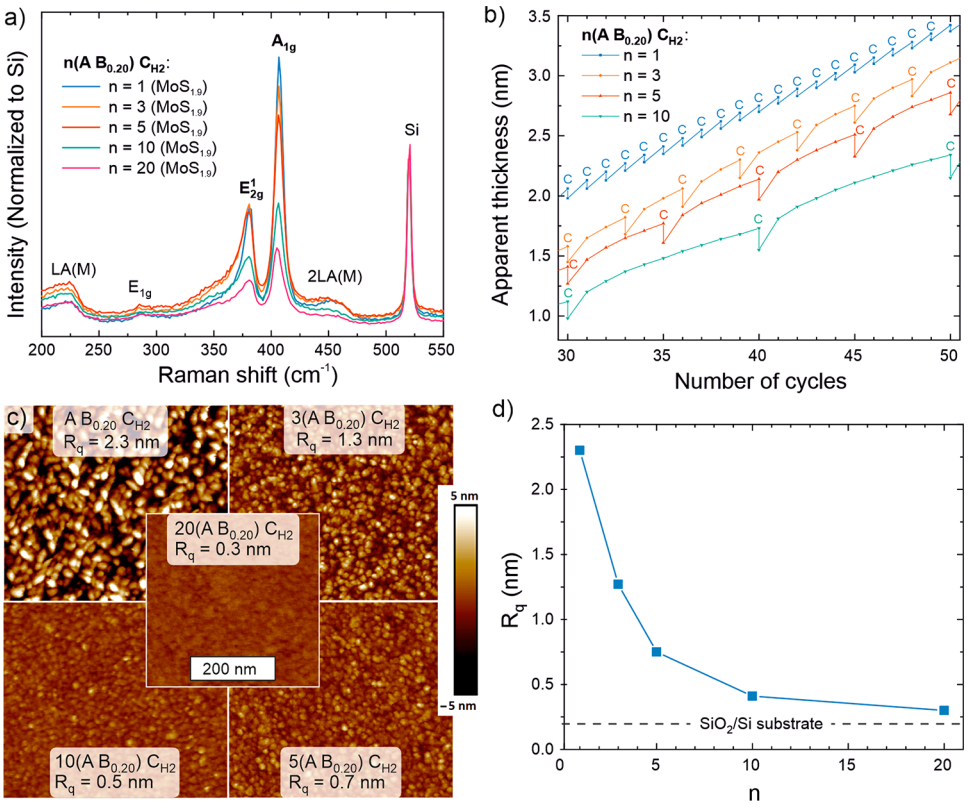


**Figure 4.** Characterization of the $n$(A $B_{0.20}$) $C_{H2}$ process: effect of $n$ on (a) crystallinity and S/Mo ratio, (b) film growth (*in situ* SE thicknesses measured after every B and C step; C steps are marked by the letter C), and (c, d) morphology and roughness (AFM). The analyzed films were 6–8 nm thick.

observed to decrease when pressure was increased (Figure S5); thus, the lowest pressure allowing for reliable striking of $H_2$ plasma (20 mTorr) was used in further experiments. The pressure dependence suggests that while H radicals likely play a major role in changing stoichiometry from $MoS_{3.5}$ to $MoS_{1.9}$, low-energy ions, such as $H_3^+$,[40] may have a beneficial effect on crystallinity.[35,41]

While the amorphous, sulfur-rich films deposited by the A $B_{0.20}$ process are smooth (Figure 1c), the crystalline $MoS_2$ films obtained with the A $B_{0.20}$ $C_{H2}$ process exhibit a rough surface (Figure 1d). Surface roughness causes charge carrier scattering,


https://doi.org/10.1021/acsami.3c02466
ACS Appl. Mater. Interfaces 2023, 15, 35565–35579

which limits electrical performance, and may lead to challenges in integration to nanoscale devices. The large roughness results from out-of-plane oriented grains or "fins" (Section 2.3.1). The edges of TMDC crystallites, including fins, are known to be more reactive compared to their basal planes, as confirmed by both DFT calculations[37] and experiments.[37,39] Fins may form through multiple pathways, for example when two laterally growing $MoS_2$ crystallites meet each other.[42] Highly reactive species generated in $H_2$ plasma can play a role in both creation and etching of fins.[42] Unless effectively removed or passivated, the highly reactive fins grow rapidly in the out-of-plane direction, resulting in rough film morphology (Figure 3b).

*2.2.2. Using $H_2$ Plasma Every n Cycles: n(A $B_{0.20}$) $C_{H2}$ Process.* We hypothesized that application of a $H_2$ plasma C step once every $n$ cycles instead of every cycle, which is denoted as $n$(A $B_{0.20}$) $C_{H2}$, may lead to smoother film morphology. The A $B_{0.20}$ cycles deposit a-$MoS_{2+x}$, which lacks the anisotropy of 2D $MoS_2$, and may therefore hinder fin growth (Figure 3a). For the $n$(A $B_{0.20}$) $C_{H2}$ process to result in c-$MoS_2$ films, periodic $H_2$ plasma exposures must be able to remove excess S and crystallize the deposited material as $MoS_2$ over the thickness of several Å deposited during $n$ A $B_{0.20}$ cycles. Raman spectroscopy and XPS suggest that this is indeed the case, as application of $H_2$ plasma every 3, 5, 10, or even 20 A $B_{0.20}$ cycles resulted in crystalline films with $MoS_{1.9}$ composition (Figure 4a).

Further insights into growth mechanisms were sought from *in situ* SE measurements performed twice every cycle, i.e., after each B and C step. In this way, the thickness changes resulting from each plasma exposure could be followed with sub-Å resolution.[43] The extracted thicknesses are best seen as apparent thicknesses due to the use of fixed c-$MoS_{1.9}$ optical constants that were determined from the end point of each deposition. Nevertheless, the apparent thickness clearly decreased after each $H_2$ plasma C step (Figure 4b and Figure S11 in the Supporting Information). This is expected, considering that more than 40% of the S atoms deposited by the $n$ A $B_{0.20}$ cycles are removed when the $H_2$ plasma step converts a-$MoS_{3.5}$ to c-$MoS_{1.9}$.

The apparent GPC in the first A $B_{0.20}$ cycle following a $H_2$ plasma C step was between 1.5 and 2.5 Å, which is much higher than the steady-state GPC of the A $B_{0.20}$ process (0.7 Å). For $n$ > 1, the GPC quickly decreased in the following A $B_{0.20}$ cycles, such that the aforementioned steady-state GPC was reached after 5−10 AB cycles. This is in line with a transition from a c-$MoS_2$ surface to an a-$MoS_{2+x}$ surface when multiple A $B_{0.20}$ cycles are applied (Figure 3d). a-$MoS_{2+x}$ is hypothesized to contain a lower density of reactive sites where the $Mo(N^tBu)_2(NMe_2)_2$ precursor can adsorb, which explains the decrease in GPC despite the increase in S/Mo stoichiometry compared to c-$MoS_2$.[39] XPS measurements confirmed that A $B_{0.20}$ cycles indeed deposit $MoS_{2+x}$ on a c-$MoS_2$ surface (Section S2.3 in the Supporting Information).

AFM showed that the surface roughness decreased with increasing $n$. The roughness of the films deposited using the A $B_{0.20}$ $C_{H2}$ process was high, with features as high as 10 nm observed for a nominally 7 nm thick film ($R_q$ = 2.3 nm, Figure 4c). TEM confirmed these features to be fins (Section 2.3.1). When $n$ was increased, the height of these features decreased together with a decreasing roughness. The roughness of 6−7 nm films deposited by using $n$ = 10 and 20 approached that of the substrate (Figure 4d). The decrease in roughness suggests hindered fin growth or formation, in line with the proposed growth mechanisms (Figure 3d).

Analysis of the Raman data shown in Figure 4a and X-ray diffraction (XRD) data in Figure S8 suggested crystallinity to decrease with increasing $n$ (see Section 2.3.1 for crystallinity analysis). Considering growth characteristics, morphology, and crystallinity, $n$ = 10 was chosen as the preferred $H_2$ plasma frequency for obtaining smooth, crystalline $MoS_2$ films.

*2.2.3. Using Ar Plasma: A $B_{0.20}$ $C_{Ar}$ Process.* $Ar^+$ ion bombardment from Ar plasma offers another route to the removal of excess sulfur from a-$MoS_{2+x}$ and subsequent crystallization. In order to obtain $Ar^+$ ions of sufficient flux and energy from our remote ICP source, low pressures ranging from 1 to 6 mTorr were used. The most efficient removal of excess S and consequently S/Mo ratios closest to 2 as well as the highest degree of crystallinity were achieved at the lowest available pressure of 1 mTorr and long exposure times of at least 60 s (Figure 5a—use of substrate biasing will be discussed below). In particular, $MoS_{2.3}$ and $MoS_{2.1}$ films deposited by using 60 and 120 s Ar plasma exposures at 1 mTorr exhibited clear Raman signatures of c-$MoS_2$ (Figure 5b). For further experiments, a 60 s Ar plasma exposure at 1 mTorr was chosen, which resulted in a GPC of 0.8 Å, a relatively smooth morphology, and high resistivity of 220 Ω cm. Further data and discussion on characterization and optimization are provided in Section S2.4 in the Supporting Information.

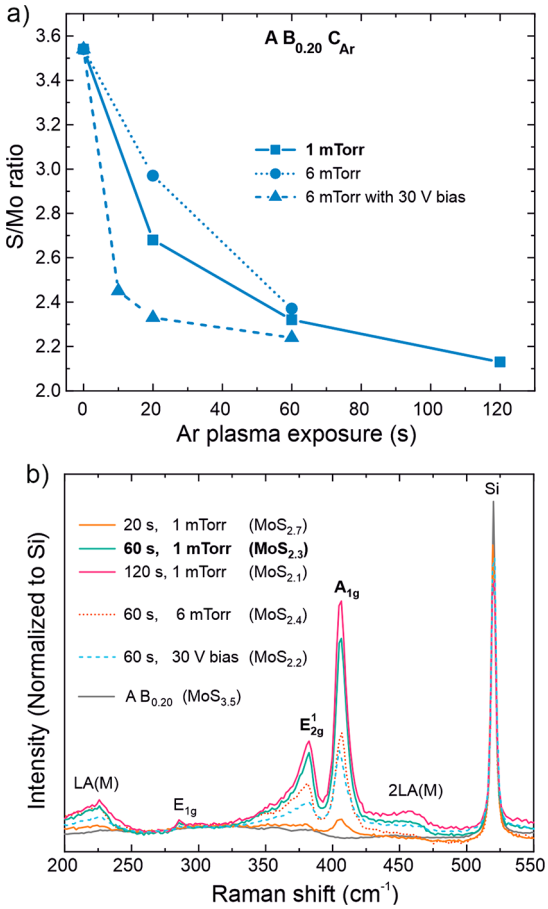


**Figure 5.** Characterization of the A $B_{0.20}$ $C_{Ar}$ process: effect of Ar plasma conditions and exposure on (a) S/Mo ratio (XPS) and (b) crystallinity (Raman spectroscopy). The films were deposited by using 140 ALD cycles at 150 °C.


https://doi.org/10.1021/acsami.3c02466
ACS Appl. Mater. Interfaces 2023, 15, 35565−35579

For an Ar plasma at 1 mTorr, we can estimate based on earlier measurements in a similar reactor[42,44−46] the mean kinetic energy of $Ar^+$ ions at 25−30 eV and the ion flux incident on the substrate at 2−4 × $10^{14}$ $cm^{-2}$ $s^{-1}$. Combining this information with Rutherford backscattering spectrometry (RBS) data on the areal density of atoms deposited allows us to estimate that on average, ∼100 $Ar^+$ ions with a mean kinetic energy of 25−30 eV are needed to remove a single S atom at the optimized 60 s Ar plasma exposure (Section S2.6 in the Supporting Information).

We explored the use of RF substrate biasing[44,47,48] to increase the energy of $Ar^+$ ions and decrease the amount of required ions and processing time. Already a 10 s exposure at 30 V substrate bias (estimated mean ion energy of 45−55 eV) resulted in efficient S removal (Figure 5a) and signs of crystallinity (Section S2.5 in the Supporting Information). However, the crystallinity as inferred from the intensity and width of the $MoS_2$ Raman modes remained low within the range of plasma exposures (10 to 60 s) and biasing voltages explored (30 to 60 V). Figure 5b shows the best identified biasing condition of 60 s exposure at a 30 V bias.

The detrimental effect of substrate biasing is likely due to ion energies exceeding a material dependent damage threshold.[44,48] Lin et al.[49] found the damage threshold of $Ar^+$ ions for a $MoS_2$ monolayer to be between 25 and 35 eV. Lu et al.[50] used 50 eV $Ar^+$ ions to selectively remove the top S layer of bulk $MoS_2$. Molecular dynamics simulations[51,52] have suggested $Ar^+$ ion sputtering thresholds of approximately 20 and 50 eV for S and Mo atoms in a $MoS_2$ monolayer. Our experiments suggest that there is also a lower energy threshold below which $Ar^+$ ions are ineffective in removing excess S. Plasma sources producing a high ion flux but low ion energies[33,53] and tailored waveform biasing[45] that can achieve accurate ion energy control are likely to be useful tools for the A $B_{0.20}$ $C_{Ar}$ and related processes.

**2.3. Comparison of Material Properties.** *2.3.1. Crystallinity, Microstructure, and Morphology.* With the A $B_{0.20}$ $C_{H2}$, 10(A $B_{0.20}$) $C_{H2}$, and A $B_{0.20}$ $C_{Ar}$ processes optimized, we proceeded to compare these to each other along with a more detailed characterization of the crystallinity, morphology, impurities, and electrical properties. In addition to these three ABC processes developed in this work, we have included data for our previously developed A $B_{0.80}$ process,[39] which also deposits crystalline films at the same temperature of 150 °C. A table comparing the properties of the three ABC processes to each other as well as to different AB processes (A $B_{0.20}$, A $B_{0.65}$, and A $B_{0.80}$) is provided in the Supporting Information (Section S3.4). This comparison highlights the improved control of the ABC approach, which significantly expands the range of film properties achieved compared with the preceding AB processes. Section S3.5 compares our processes and film characteristics to those in the literature. Finally, besides the selected three, other evaluated ABC processes including different plasma steps ($H_2S$/Ar, $H_2$, and Ar) added to the A $B_{0.80}$ process are described in the Supporting Information (Section S5).

For a fair comparison of crystallinity, 5 nm thick films were deposited by using each of the processes. Deconvolution of Raman spectra in the region of the in-plane $E^1_{2g}$ and the out-of-plane $A_{1g}$ $MoS_2$ modes revealed clear differences between the processes (Figure 6a). The width of these modes is indicative of the crystalline quality: $MoS_2$ monolayers exfoliated from high-quality bulk material yield sharp peaks

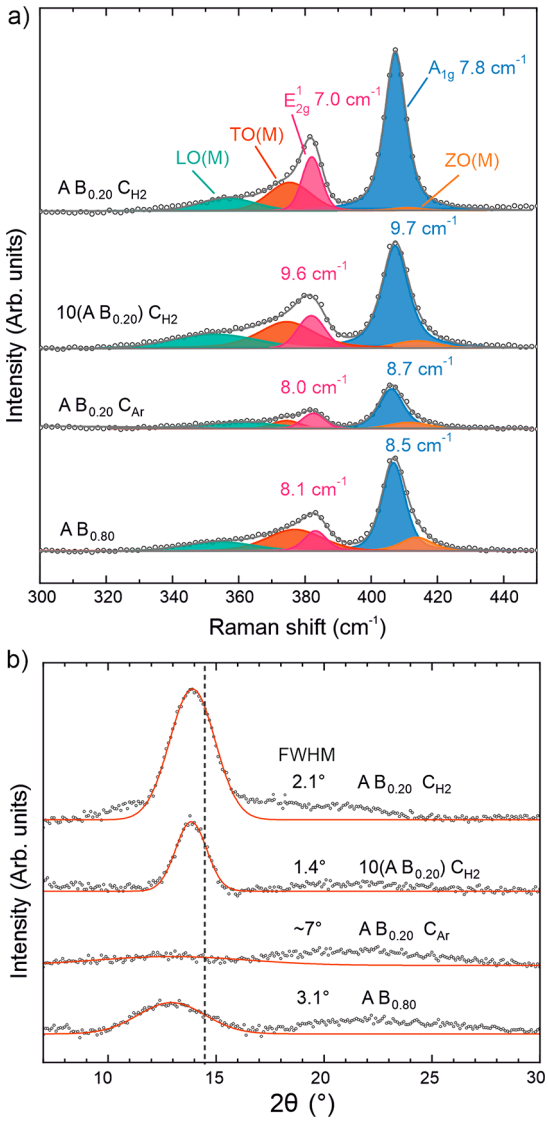


**Figure 6.** Crystallinity of ∼5 nm films deposited at 150 °C by using different ABC processes. (a) Raman spectra with peak deconvolution and fwhm's for the $E^1_{2g}$ and $A_{1g}$ peaks shown. (b) $\theta$−$2\theta$ X-ray diffractograms after background removal showing also Gaussian peaks fitted to the (0002)$MoS_2$ reflection and their fwhm's. The dashed line shows the reference position (14.4° $2\theta$; JCDPS-ICDD powder diffraction file 00−037−1492). The broad peak centered at approximately 22° $2\theta$ originates from the 450 nm thick $SiO_2$ layer of the substrate. The data were offset vertically for clarity in both panels.

(full-width at half-maximum, fwhm ≈3−4 $cm^{-1}$), while the peaks broaden with increasing defectivity.[54] For films of similar thickness, we have also observed a correlation of increased Raman intensity with improved crystallinity. Disorder-activated LO(M), TO(M), and ZO(M) modes provide another signature of defectivity, as the intensity ratio of these modes to $E^1_{2g}$ and/or $A_{1g}$ increases with increasing defect density.[54] All of these metrics suggest that the best crystalline quality was obtained using the A $B_{0.20}$ $C_{H2}$ process, which is also clearly improved over the A $B_{0.80}$ process. The $E^1_{2g}$ fwhm of the A $B_{0.20}$ $C_{H2}$ process is comparable to or even lower compared to $MoS_2$ deposited using other methods at 300−500 °C (Figure S29 in the Supporting Information). Applying $H_2$ plasma only every 10 cycles (i.e., 10(A $B_{0.20}$) $C_{H2}$ process) resulted in


https://doi.org/10.1021/acsami.3c02466
ACS Appl. Mater. Interfaces 2023, 15, 35565−35579

clearly higher defectivity compared to that of the A $B_{0.20}$ $C_{H2}$ process. The A $B_{0.20}$ $C_{Ar}$ plasma process yielded fwhm's between the two $H_2$ plasma based processes but much lower peak intensities, which may be due to its smaller crystallite size discussed below.

Complementary information on crystallinity was obtained using X-ray diffraction (XRD) in symmetric $\theta$-$2\theta$ geometry (Figure 6b) which probes crystalline planes parallel to the substrate surface. The (0002) reflection originating from $MoS_2$ basal planes was observed for all of the processes at a similar position, slightly below that of a bulk reference. Only the A $B_{0.80}$ process showed a clear shift to smaller angles, which suggested a larger spacing between the basal planes. This may be due to the large amount of hydrogen (~20 at. %) incorporated.[39]

The intensity of the (0002) reflection, which can be taken as a measure of crystalline order (basal planes parallel to the substrate), was the highest for the A $B_{0.20}$ $C_{H2}$ process, followed by the 10(A $B_{0.20}$) $C_{H2}$ and A $B_{0.80}$ processes. The peak intensity for the A $B_{0.20}$ $C_{Ar}$ process was very low. The width of the peak was the narrowest for the 10(A $B_{0.20}$) $C_{H2}$ process (fwhm = 1.4°); otherwise, it increased in the order of decreasing intensity. As peak broadening is caused by limited crystal size in the direction perpendicular to the substrate, which cannot exceed film thickness, the narrowest peak produced by the 10(A $B_{0.20}$) $C_{H2}$ process may be due to its smooth surface and underestimation of thickness by SE as discussed below with the TEM images.

Cross-sectional transmission electron microscopy (TEM) was used to complement Raman and XRD for crystallinity analysis (Figure 7, additional images in Figures S22–S24). The images show that for the A $B_{0.20}$ $C_{H2}$ process, the basal planes of the majority of the $MoS_2$ crystallites were oriented approximately parallel to the substrate (Figure 7a). The shown film mainly consisted of 6–8 ML thick $MoS_2$ crystallites resulting in a film thickness of 4.4 ± 0.5 nm (average of 12 locations), in good agreement with SE thickness (4.6 nm). In addition, some fins oriented at random angles were observed as is common for (PE)ALD TMDCs.[31,36,55,56] The film grown by using the 10(A $B_{0.20}$) $C_{H2}$ process appeared more disordered, which may be due to its smaller crystallite size or a larger spread in the crystallite orientation (Figure 7b). Remarkably, the film appeared very smooth with no visible fins. The thickness measured from the TEM image, 5.9 ± 0.4 nm, was much larger than the 4.6 nm measured by SE. The highest disorder of the A $B_{0.20}$ $C_{Ar}$ films as suggested by Raman and XRD was also apparent in the TEM images. Nevertheless, the film appeared to be completely crystallized (Figure 7c). Some fins, albeit of a lower height compared to the A $B_{0.20}$ $C_{H2}$ process, are visible in Figure 7c. This shows that the 10(A $B_{0.20}$) $C_{H2}$ process prevents fins more efficiently than the A $B_{0.20}$ $C_{Ar}$ process. The TEM thickness of 4.6 ± 0.8 nm, agrees well with SE (4.8 nm). Thus, the SE models and extracted optical constants appear adequate for the A $B_{0.20}$ $C_{H2}$ and A $B_{0.20}$ $C_{Ar}$ processes (Figure S27), whereas for the 10(A $B_{0.20}$) $C_{H2}$ process, we were unable to develop an accurate model even with the TEM thickness information.

The lateral grain size was estimated by manually identifying crystallites from the TEM images, yielding 17 ± 5, 11 ± 5, and 6 ± 2 nm for the A $B_{0.20}$ $C_{H2}$, 10(A $B_{0.20}$) $C_{H2}$, and A $B_{0.20}$ $C_{Ar}$ processes (Figure 7). Although the absolute values carry some uncertainty due to the difficulty in unambiguously identifiying grain boundaries, the trend is in agreement with Raman, TEM,

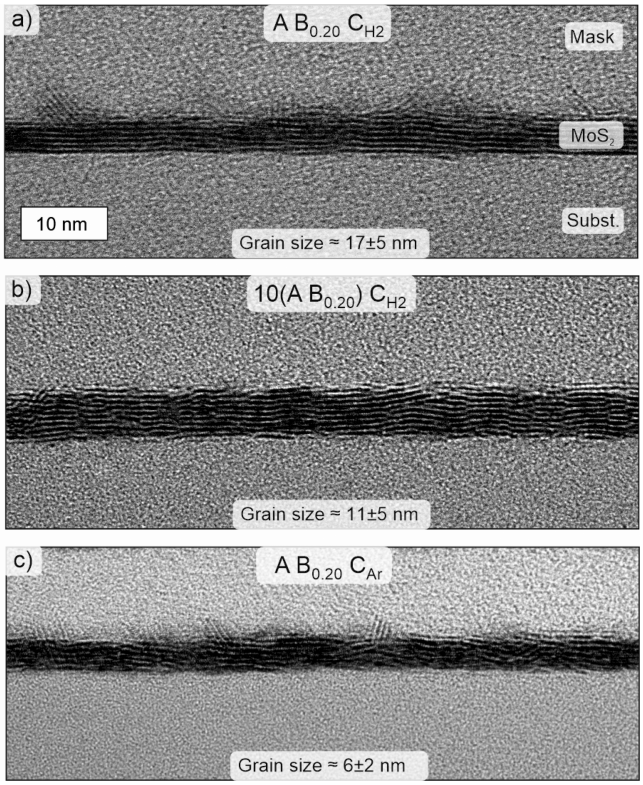


**Figure 7.** Microstructure of ~5 nm $MoS_2$ films deposited using (a) A $B_{0.20}$ $C_{H2}$, (b) 10(A $B_{0.20}$) $C_{H2}$, and (c) A $B_{0.20}$ $C_{Ar}$ processes as analyzed by cross-sectional TEM. Grain sizes estimated from multiple images are also indicated (average ± standard deviation).

and XRD analysis. These grain sizes are comparable to $MoS_2$ films deposited by ALD and CVD at 200–400 °C (Table S10). The crystallite orientation was quantified from the TEM images, confirming the lowest orientation spread with respect to the substrate surface for the A $B_{0.20}$ $C_{H2}$ process followed by the 10(A $B_{0.20}$) $C_{H2}$ and A $B_{0.20}$ $C_{Ar}$ processes (Figure S25).

The morphology of the films deposited by using different processes was further studied by AFM. Figure 8a shows AFM images of ~5 nm thick films. The already discussed drastic difference between the two $H_2$ plasma based processes is clear: the A $B_{0.20}$ $C_{H2}$ process produces the roughest films out of all the studied processes, while the 10(A $B_{0.20}$) $C_{H2}$ process produces the smoothest films.

The evolution of morphology and roughness as a function of film thickness also greatly varies between the processes (Figure 8b—see Figure S26 for images). For the A $B_{0.20}$ $C_{H2}$ process, fins begin to form and grow already during the first cycles (i.e., below 1 nm thickness), resulting in a rapid and continuous increase of roughness with increasing thickness. In stark contrast, for the 10(A $B_{0.20}$) $C_{H2}$ process, surface roughness is independent of film thickness, showing that this process allows deposition of smooth ($R_q \approx 0.5$ nm) films up to a thickness of at least 7 nm. The films deposited using the A $B_{0.20}$ $C_{Ar}$ process reach a moderate roughness ($R_q \approx 1.0$ nm) with clearly visible surface features already at a thickness of 3 nm. However, increasing the thickness beyond 10 nm does not increase the roughness appreciably, despite an apparent lateral growth of the surface features. Thus, although comparable to the A $B_{0.80}$ process at a thickness of ≤7 nm, at higher thicknesses the A $B_{0.20}$ $C_{Ar}$ process produces smoother films. Linking this result to the TEM images suggests that fins form for the Ar plasma


https://doi.org/10.1021/acsami.3c02466
ACS Appl. Mater. Interfaces 2023, 15, 35565–35579

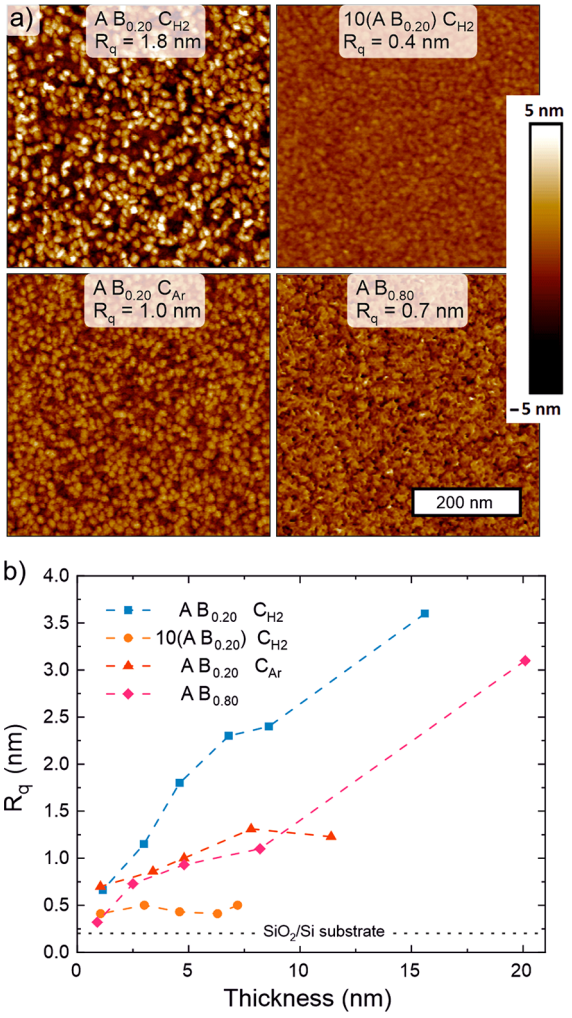


**Figure 8.** Morphology of $MoS_2$ films deposited at 150 °C using different ABC processes (data for A $B_{0.80}$ from ref 39 shown for reference). (a) AFM images of ∼5 nm thick films and (b) evolution of roughness as a function of thickness.

based process, but they do not easily grow as they do for the A $B_{0.20}$ $C_{H2}$ and A $B_{0.80}$ processes (Figure 3).

*2.3.2. Film Composition.* The S/Mo stoichiometry and chemical environment of Mo and S were analyzed by using core-level X-ray photoelectron spectra. As discussed in detail with the optimization of each process, the $H_2$ plasma based processes deposit practically stoichiometric $MoS_2$, while the Ar plasma is less efficient in removing excess S and results in slightly overstoichiometric films ($MoS_{2.3}$).

Using the A $B_{0.20}$ $C_{H2}$ process as an example, the Mo 3d region mainly consisted of a doublet attributed to $Mo^{4+}$ in $MoS_2$ with a Mo $3d_{5/2}$ binding energy (BE) of 229.6 eV (Figure 9a, see Table S7 in the Supporting Information for more details of the peak deconvolution). Minor doublets attributed to $Mo^{5+}$ and $Mo^{6+}$ species at Mo $3d_{5/2}$ BEs of 231.5 and 232.9 eV are likely a result of oxidation of the films in air.[57−59] The observed BEs agree well with average literature values of 229.3 ± 0.5 eV for $MoS_2$ and 232.7 ± 0.3 eV for $MoO_3$.[60] The Mo 3d region was very similar for all of the ALD processes.

S 2s region overlaps with Mo 3d, and can be described with one singlet attributed to $S^{2-}$ in $MoS_2$ (BE = 226.8 eV). For the A $B_{0.20}$ $C_{Ar}$ process, a minor additional contribution at approximately 228 eV was observed. The S 2p region was analyzed for further information about the S species present (Figure 9b). For the A $B_{0.20}$ $C_{H2}$ process, this could be fit well with a doublet attributed to $S^{2-}$ in $MoS_2$, the S $2p_{3/2}$ BE of 162.4 eV being in good agreement with literature (BE = 162.3 ± 0.6 eV).[60] The measured S 2p spectrum was practically identical for the A $B_{0.20}$ $C_{H2}$, 10(A $B_{0.20}$) $C_{H2}$, and A $B_{0.80}$ processes, which also share a similar stoichiometry. For the more sulfur rich $MoS_{2.3}$ films deposited using the A $B_{0.20}$ $C_{Ar}$ process, a low intensity doublet at a higher BE (163.4 eV for S $2p_{3/2}$) was observed, which is attributed mainly to the $S_2^{2-}$ species present in sulfur-rich amorphous $MoS_{2+x}$. Amorphous $MoS_{2+x}$ contains sulfur in many different bonding environments with partially overlapping BEs as discussed in the literature,[61,62] making unambiguous assignment to different S species challenging.

The film stoichiometry was confirmed by Rutherford backscattering spectrometry (RBS) measurements, which were in good agreement with the XPS (Table 1). RBS together with elastic recoil detection analysis (ERD) was also used to analyze film impurities. The A $B_{0.20}$ and A $B_{0.80}$ processes are shown for reference along with the analyzed A $B_{0.20}$ $C_{H2}$ and A $B_{0.20}$ $C_{Ar}$ process. Although the 10(A $B_{0.20}$) $C_{H2}$ process was not analyzed, we expect it to result in a composition resembling the A $B_{0.20}$ $C_{H2}$ process.

The nitrogen content from incorporated precursor ligands was low for all processes, 0.5−1.4 at. %. Oxygen was observed in low concentrations for the processes using a $B_{0.20}$ step, 0.8−1.4 at. %, while clearly more oxygen was detected for the A $B_{0.80}$ process (6 at. %). As O may result from postdeposition oxidation in air or residual impurities in the ALD reactor, this suggests higher resistance to oxidation for the films deposited using the ABC processes, which may be linked to their lower H concentration. Up to 22 at. % H was incorporated using high $H_2$ flow ratios in B step (A $B_{0.80}$). The processes based on a $B_{0.20}$ step incorporated less H. Approximately 6 at. % of H was found in the amorphous sulfur rich films deposited by the A $B_{0.20}$ process, which increased modestly to 9 at. % when a $H_2$ plasma C step was added (A $B_{0.20}$ $C_{H2}$). Using an Ar plasma C step instead (A $B_{0.20}$ $C_{Ar}$) decreased the H content to as little as 2.3 at. %. As our previous work identified H as a dopant, decreasing the H content in the films gives promise for better semiconductor properties, namely, lower carrier densities and higher mobilities.

*2.3.3. Electrical Properties.* Motivated by the decrease of the H content in the films prepared by the newly developed ABC processes, we investigated their electrical properties and compared them to the previously developed A $B_{0.80}$ process, which yields the best electrical performance out of low-temperature (<200 °C) AB processes.[39] The ABC processes resulted in considerably higher four-point-probe (FPP) resistivities compared to the A $B_{0.80}$ process (∼0.3 Ω cm), ranging from approximately 10 Ω cm for both of the $H_2$ plasma processes to ∼200 Ω cm for the A $B_{0.20}$ $C_{Ar}$ process. These resistivity values were reached for films at least 5−7 nm in thickness. Thinner films exhibited higher resistivities, likely due to increased scattering of charge carriers at the interfaces as well as at grain boundaries (Figure S28).

AC Hall effect measurements were performed to understand the origin of the resistivity changes. Carrier densities of both of the $H_2$ plasma based processes were found to be 3 orders of magnitude lower compared to the A $B_{0.80}$ process, i.e., in the range of ∼1−3 × $10^{18}$ $cm^{-3}$ (see Section S3.3 in the


https://doi.org/10.1021/acsami.3c02466
ACS Appl. Mater. Interfaces 2023, 15, 35565−35579

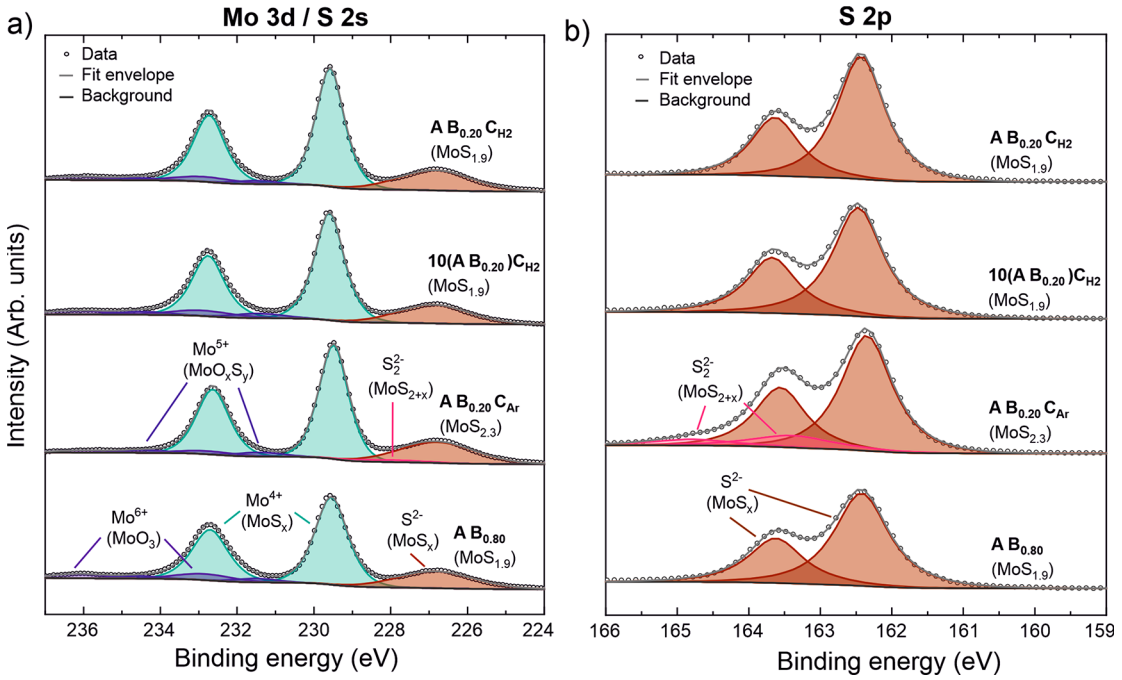


**Figure 9.** XPS spectra of (a) Mo 3d/S 2s and (b) S 2p core levels of $MoS_2$ films deposited by using different ABC processes and 140 ALD cycles at 150 °C. S/Mo stoichiometry is indicated, and the A $B_{0.80}$ process is shown for comparison. The spectra were vertically offset for clarity.

**Table 1. Elemental Composition of ~50 nm Thick $MoS_x$ Films Deposited by Using Different Processes**[a]

| Process | S/Mo (RBS) | S/Mo (XPS) | H (at. %) | C (at. %) | N (at. %) | O (at. %) | Ar (at. %) |
|---|---|---|---|---|---|---|---|
| A $B_{0.20}$ | 3.70 ± 0.13 | 3.54 ± 0.04 | 6.3 ± 0.5 | <dl | 0.5 ± 0.2 | 0.8 ± 0.2 | <dl |
| A $B_{0.20}$ $C_{H2}$ | 1.95 ± 0.07 | 1.89 ± 0.02 | 9.0 ± 0.7 | <dl | 0.7 ± 0.2 | 1.4 ± 0.4 | <dl |
| A $B_{0.20}$ $C_{Ar}$ | 2.30 ± 0.08 | 2.32 ± 0.02 | 2.3 ± 0.2 | <dl | 1.4 ± 0.4 | 1.2 ± 0.4 | 0.18 ± 0.05 |
| A $B_{0.80}$ | 1.83 ± 0.07 | 1.89 ± 0.02 | 22 ± 2 | <dl | 1.0 ± 0.3 | 6 ± 2 | 0.07 ± 0.06 |

[a]Composition was analyzed by RBS (Mo, S, C, N, O, Ar) and ERD (H). Detection limits (dl) are approximately 7 and 0.05 at. % for C and Ar, respectively. S/Mo ratios determined by XPS are shown for comparison. The RBS and ERD uncertainties comprise known systematic and statistical uncertainties, while the XPS uncertainty represents statistical uncertainty only. The data for the A $B_{0.20}$ and A $B_{0.80}$ processes has been published in ref 39.

Supporting Information for detailed results and further discussion). Using the A $B_{0.20}$ $C_{Ar}$ process, a further decrease in carrier density to ~$6 \times 10^{16}$ $cm^{-3}$ was achieved. The carrier densities decrease with decreasing hydrogen concentration, in line with hydrogen being a dopant in the films.[39] The relationship is not linear, however, suggesting that other factors including chemical bonding of H, other impurities (O, N), crystallinity, and morphology may also affect the electrical properties (Section S3.3).

Furthermore, the Hall mobility of the three ABC processes was an order of magnitude higher compared to the A $B_{0.80}$ process, that is, approximately 0.3 $cm^2$ $V^{-1}$ $s^{-1}$. The improved mobility may be due to decreased charge carrier scattering as a result of both a lower carrier concentration and improved crystallinity compared to the A $B_{0.80}$ process. The decreased carrier densities and increased mobilities over previous work give promise for semiconductor applications, especially plastic-based flexible electronics requiring a very low thermal budget. The smooth morphology of the 10(A $B_{0.20}$) $C_{H2}$ process appears to be particularly suitable for electronics.

**2.4. Application in Electrocatalysis.** Electrocatalytic HER is a commonly explored TMDC application, which benefits from the presence of defects such as crystallite edges and vacancies that have been identified as catalytically active sites.[12,14,15] Here, we deposited approximately 7 nm thick $MoS_2$ films on glassy carbon (GC) substrates by using our three ABC processes. Figure 10 shows cyclic voltammograms (CVs) of the different catalysts as well as the bare GC substrate

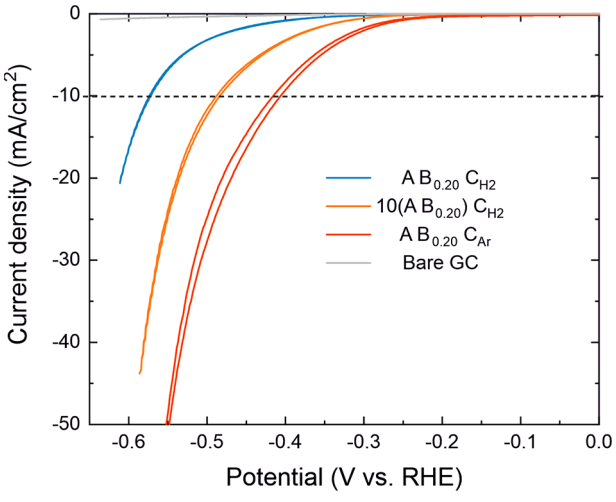


**Figure 10.** CVs of $MoS_2$ films deposited on GC and the bare substrate used as a reference. The fifth CV scan recorded for each sample is shown.


https://doi.org/10.1021/acsami.3c02466
ACS Appl. Mater. Interfaces 2023, 15, 35565−35579

recorded in 0.5 M $H_2SO_4$. The most commonly used activity metric is the overpotential $\eta$ required to reach a current density of 10 mA/cm$^2$, which we denote $\eta_{10}$.[63,64] As the thermodynamic potential for HER is 0 V versus RHE, this is equal to the absolute value of the (negative) potential applied at this current density. The lowest $\eta_{10}$ value of 406 mV was observed for the A $B_{0.20}$ $C_{Ar}$ process followed by the 10(A $B_{0.20}$) $C_{H2}$ (484 mV) and A $B_{0.20}$ $C_{H2}$ (573 mV) processes (Figure 10 and Table 2). The HER currents measured for all of the samples were considerably higher compared with the bare substrate, confirming that our $MoS_2$ films are indeed catalytically active. Tafel analysis provides a complementary view to HER activity, as a low Tafel slope indicates that high current densities that are required for practical electrolyzers can be achieved at reasonable overpotentials.[16] The Tafel slopes (Table 2 and Figure S31) of the 10(A $B_{0.20}$) $C_{H2}$ (115 mV/dec) and A $B_{0.20}$ $C_{Ar}$ (123 mV/dec) processes were lower compared to those of the A $B_{0.20}$ $C_{H2}$ process (165 mV/dec), which also required the highest overpotential.

**Table 2. Summary of HER Catalyst Metrics Extracted from Electrochemical Measurements**

| Process | $\eta_{10}$ (mV) | Tafel slope (mV/dec) | $C_{dl}$ ($\mu$F/cm$^2$) |
|---|---|---|---|
| A $B_{0.20}$ $C_{H2}$ | 573 | 165 | 18 |
| 10(A $B_{0.20}$) $C_{H2}$ | 484 | 115 | 36 |
| A $B_{0.20}$ $C_{Ar}$ | 406 | 123 | 135 |

To rationalize the differences in activity between the different $MoS_2$ catalysts, double layer capacitance ($C_{dl}$) of the films was measured by scanning potential in the non-Faradaic region at varying scan rates (see Table 2 and Figure S33 for the measured data and fits). The measured $C_{dl}$ values increased in the order of increasing HER activity (decreasing $\eta_{10}$). $C_{dl}$ is proportional to the density of double layer adsorption sites, which appears to correlate here with the density of HER active sites. Indeed, normalizing the current densities by $C_{dl}$ brought the activities of different samples closer to each other (Figure S32 in the Supporting Information).

The lowest $C_{dl}$ produced by the A $B_{0.20}$ $C_{H2}$ process may result from its largest grain size and orientation of most of the $MoS_2$ crystallites parallel to the substrate (Figure 7a). The fins, although resulting in a large roughness, only provide a limited amount of active edge sites due to their relatively low surface coverage, in agreement with previous studies on PEALD $WS_2$.[37] Although smoother on the surface, the 10(A $B_{0.20}$) $C_{H2}$ films may provide a higher accessible edge site density due to a smaller grain size and larger spread in the crystallite orientation. In addition, the more disordered structure suggested by Raman and TEM may indicate an increased number of active (defect) sites on the basal planes. Combining the clearly highest $C_{dl}$ together with the lowest $\eta_{10}$ as well as the S-rich composition suggests that the A $B_{0.20}$ $C_{Ar}$ films contain disordered c-$MoS_2$ domains and potentially even active-site-rich nanoscale a-$MoS_{2+x}$ clusters.[65,66] This makes the Ar plasma based process the preferred choice for HER.

The overpotentials and Tafel slopes of our three catalysts fall in the range reported for nanocrystalline, relatively smooth $MoS_2$ thin films on flat, inert substrates.[31,67,68] This greatly exceeds the activity of bulk $MoS_2$ ($\eta_{10}$ > 1000 mV),[68] but falls short of the best $MoS_2$ catalysts taking advantage of, for example, vacancy engineering and strain, which can achieve $\eta_{10}$ approaching 150 mV (refs 13, 15, and 69 and references therein). As shown by the activity differences among our three processes, we envision that ABC type PEALD processes can be optimized for defect engineering by rationally controlling different plasma species. Depositing $MoS_2$ on high-surface area substrates, which is one of the unique strengths of ALD, can be used to improve performance toward practical catalysts. Doping is another strategy yielding improvements in the HER performance of $MoS_2$,[14,15] which can be implemented in (PE)ALD to improve catalytic activity.

## 3. CONCLUSIONS

We developed a toolbox of advanced PEALD processes depositing wafer-scale polycrystalline $MoS_2$ films with rationally controlled properties and thickness at 150 °C, one of the lowest temperatures achieved in the literature. Using two individually tailored plasma exposures in an "ABC cycle" greatly improves the control over film properties compared to conventional "AB" type PEALD processes with a single plasma exposure per cycle. Our approach gives ample flexibility in process design via control of plasma parameters such as plasma

**Table 3. Summary of Selected Film Characteristics of the Three ABC Processes**

| | A $B_{0.20}$ $C_{H2}$ | 10(A $B_{0.20}$) $C_{H2}$ | A $B_{0.20}$ $C_{Ar}$ |
|---|---|---|---|
| *Composition:* | | | |
| S/Mo ratio[a] | 1.9 | 1.9 | 2.3 |
| Impurities (at. %)[b] | H: 9, O: 1.4, N: 0.7 | | H: 2.3, O: 1.2, N: 1.4, Ar: 0.2 |
| *Film growth:* | | | |
| GPC (Å)[c] | 1.1 | 0.4 | 0.8 |
| Nonuniformity (4 in.)[c] | 2.4% | | 2.2% |
| *Structure:* | | | |
| Crystallinity[d] | Highest | Medium | Lowest |
| Grain size (nm)[e] | 17 ± 5 | 11 ± 5 | 6 ± 2 |
| Roughness (nm)[f] | 2.3 | 0.5 | 1.3 |
| *Electrical properties*[g] | | | |
| $n$ (cm$^{-3}$) | 1.3 ± 0.7 × 10$^{18}$ | 2.6 ± 1.4 × 10$^{18}$ | 6 ± 3 × 10$^{16}$ |
| $\mu$ (cm$^2$ V$^{-1}$ s$^{-1}$) | 0.25 ± 0.15 | 0.30 ± 0.13 | 0.36 ± 0.17 |
| *HER performance* | | | |
| $\eta_{10}$ (mV) | 573 | 484 | 406 |

[a]XPS and RBS. [b]RBS and ERD. [c]SE, averaged over 140 cycles. [d]Raman, XRD, and TEM. [e]TEM. [f]AFM, 7 nm thickness. [g]AC Hall effect.


https://doi.org/10.1021/acsami.3c02466
ACS Appl. Mater. Interfaces 2023, 15, 35565−35579

Table 4. Plasma Conditions Used for Different Processes in the B and C steps.[a]

| Plasma step | Exposure time (s) | $H_2S$ flow rate (sccm) | $H_2$ flow rate (sccm) | Ar flow rate (sccm) | p (mTorr) | ICP P (W) |
|---|---|---|---|---|---|---|
| $B_{0.20}$ | 20 | 8 | 2 | 40 | 6 | 100 |
| $B_{0.80}$ | 20 | 2 | 8 | 40 | 6 | 100 |
| $C_{H2}$ | 20 (5−60) | 0 | 100 | 0 | 20 (20−300) | 100 |
| $C_{Ar}$ | 60 (20−120) | 0 | 0 | 10 (10−40) | 1 (1−6) | 100 (100−500) |

[a]The first number represents optimized conditions for each process, while the range of parameters evaluated is indicated in parentheses.

gases, pressure, power, exposure time, and order and periodicity of different plasma steps. We have focused on three processes, where $H_2$ or Ar plasma exposure is used to remove excess sulfur incorporated into the films from $H_2S$ plasma. The choice of either Ar or $H_2$ has a strong effect on film properties as summarized in Table 3: while $H_2$ plasma yields more crystalline films, these films are usually rough and contain approximately 10 at. % H. Intriguingly, applying the $H_2$ plasma step only every 10 cycles results in smooth, crystalline films. We explain this to be a result of growth of smooth a-$MoS_{2+x}$ followed by periodic removal of excess S. Using Ar plasma yields more disordered films compared to $H_2$ plasma but also alleviates H incorporation to 2 at. % and consequently decreases the level of doping. Compared to AB processes, we can substantially decrease the carrier density of our $MoS_2$ from $10^{21}$ to $10^{16}$−$10^{18}$ $cm^{-3}$ along with an at least order of magnitude increase in Hall mobility up to 0.3 $cm^2\ V^{-1}\ s^{-1}$. These results combined with the plastic-compatible deposition temperatures make our processes interesting for flexible electronics. The smooth morphology resulting from $H_2$ plasma applied every 10 cycles (10(A $B_{0.20}$) $C_{H2}$) appears particularly suitable for (opto)electronics. The control of morphology and exposure of fins and grain boundaries achieved by different plasmas is of interest for flexible gas sensors. The different ABC processes exhibit different levels of activity for electrocatalytic HER, which can be linked to the film morphology and crystallinity. The Ar plasma process displays the highest HER activity stemming from active sites, such as crystallite edges and other defects. The flexibility, scalability, and low thermal budget of our approach gives ample opportunities for further expanding the ABC process toolbox to tailor $MoS_2$ and other TMDCs for electronics, catalysis, and other applications.

## 4. EXPERIMENTAL SECTION

**4.1. Film Deposition.** $MoS_x$ thin films were deposited by PEALD using an Oxford Instruments FlexAL PEALD reactor equipped with a remote 13.56 MHz inductively coupled plasma (ICP) source. The chamber was pumped with a turbomolecular pump capable of reaching a base pressure of $1 \times 10^{-6}$ Torr. Unless otherwise noted, the table and wall temperatures were set to 150 °C, meaning that the reactor acted as a hot wall reactor with a substrate temperature of 150 °C. For experiments at higher temperatures, only the table temperature was increased, while for lower temperatures both the table and wall temperatures were set to the indicated temperature. The films were deposited on silicon(100) substrates with a 450 nm wet thermal $SiO_2$ layer on top (Siegert Wafer). In most cases, approximately $1 \times 1$ to $3 \times 3$ $cm^2$ coupons were used on an 8 in. carrier wafer that was introduced into the chamber through a load lock. After transfer, the substrates were let to thermally equilibrate for 5 min before starting the deposition.

ABC type PEALD processes were mostly used in this work. The A step consisted of 6 s of $Mo(N^tBu)_2(NMe_2)_2$ dosing at 200 mTorr, the B step of 20 s $H_2S/H_2/Ar$ plasma exposure at 6 mTorr, and the C step of an additional Ar or $H_2$ plasma exposure (conditions indicated in Table 4). In addition, a purging/pumping step was included after every A, B, and C step. After an A step, both a 6 s purging step with 300 sccm Ar flow and 4 s pumping without gas flows were used, while after B and C steps only the 6 s Ar purging step was employed. Additional, 4 and 5 s long pressure and gas flow stabilization steps preceded the Mo precursor and plasma pulses, respectively. Figure S1 in the Supporting Information shows the pulsing schemes used for different processes.

The processes are denoted A $B_x$ $C_y$ where $x$ represents the $H_2$ flow ratio in the B step according to eq 1 and y represents the plasma feed gas(es) for the C step. In most of the processes, a C step was added to each ALD cycle. Adding a C step only every $n$ cycles instead of every cycle, is denoted $n$(A $B_x$) $C_y$. Unless otherwise noted, both the B and C steps are plasma steps.

The $Mo(N^tBu)_2(NMe_2)_2$ (98%, Strem Chemicals) precursor was heated to 50 °C in an external canister and supplied to the chamber by Ar flow through delivery lines that were heated to 70 °C to prevent condensation. The flow rates of $H_2S$ (99.5%), $H_2$ (99.999%), and Ar (99.999%) gases supplied by Linde gas were controlled by mass flow controllers. The pressure was controlled either by gas flows (1−20 mTorr) or an automatic butterfly valve (36−300 mTorr).

Experiments using RF substrate biasing[44,47,48] were performed to increase energy of $Ar^+$ ions impinging on the surface as discussed in the Supporting Information (Sections S2.5, S2.6).

**4.2. Film Characterization.** Film thicknesses were measured by spectroscopic ellipsometry (SE). During most of the depositions, the reactor was equipped with an *in situ* SE, either M-2000FI (spectral range of 0.7−5.0 eV) or M-2000F (spectral range of 1.2−5.0 eV) by J.A. Woollam. Typically, film thickness was measured every 10 cycles. For evaluation of growth mechanisms, measurements were performed after each B and C step. For depositions without an *in situ* SE, film thicknesses were measured *ex situ* after deposition using a variable angle J.A. Woollam M-2000U instrument (spectral range of 1.2−6.5 eV, angles 65, 75, and 85°). The SE modeling procedure was described in our previous work.[39] A B-spline model with 0.3 eV resolution was used to describe the $MoS_2$ films.

*Ex situ* uniformity mapping was performed using a J.A. Woollam M-2000 instrument (spectral range 1.2−3.3 eV) equipped with an automated mapping stage. A circular pattern excluding areas close to the wafer edges was used.

Film morphology was examined by scanning electron microscopy (SEM, Zeiss Sigma) using an InLens detector and acceleration voltage of 3 kV. Additionally, morphology and surface roughness were analyzed by atomic force microscopy (AFM, Bruker Dimension Icon) in PeakForce Tapping based ScanAsyst mode in air. Probes with a nominal spring constant of 0.4 N/m and a tip radius of 2 nm were used (ScanAsyst-Air, Bruker). Surface roughness was calculated as root-mean-square ($R_q$) value from 500 × 500 nm images after first order flattening using Bruker Nanoscope 2.0 software.

Film crystallinity was evaluated by Raman spectroscopy (Renishaw inVia confocal Raman microscope) equipped with a 514 nm laser, 50× objective (NA = 0.75), and 1800 lines/mm grating. Six spectra using 10 s accumulation time each were collected for each sample. Incident laser power was estimated to be 0.6 mW on the sample (100 mW laser with a 1% neutral density filter, accounting for optical losses). All of the presented spectra were normalized to the intensity (area) of the Si mode at 520 $cm^{-1}$. For deconvolution of the $A_{1g}/E^1_{2g}$ region, five Pseudo-Voigt peaks were fitted in the 300−450 $cm^{-1}$ range. X-ray diffraction (XRD) measurements complementing the Raman analysis were performed in symmetric $\theta$−$2\theta$ geometry using a Bruker D8 Discover diffractometer equipped with a Cu X-ray tube


https://doi.org/10.1021/acsami.3c02466
ACS Appl. Mater. Interfaces 2023, 15, 35565−35579

(K$\alpha$ $\lambda$ = 1.54 Å). Background was removed by fitting a cubic spline function to the data.

Film composition was analyzed by X-ray photoelectron spectroscopy (XPS) using a Thermo Scientific K-Alpha spectrometer equipped with a monochromatic Al K$\alpha$ source ($h\nu$ = 1486.6 eV) focused to a 400 $\mu$m spot on the sample. An electron flood gun was used during the measurements to minimize the charging effects. The binding energies were referenced by setting the adventitious carbon derived C−C/C-H component of the deconvoluted C 1s peak to 284.8 eV. A pass energy of 20 eV was used for high-resolution spectra. Peak deconvolution was performed using Avantage software (Thermo Scientific) using Gaussian−Lorentzian (30% Lorentzian) sum functions with a Shirley-type background.

Rutherford backscattering spectrometry (RBS) and elastic recoil detection (ERD) measurements were performed by Detect 99 B.V. (Eindhoven, The Netherlands) using a 2 MeV $He^+$ beam. RBS was used to determine the absolute areal atom density, S/Mo stoichiometry, and impurities besides hydrogen. Hydrogen concentration was determined by ERD. The reported uncertainties take into account known systematic and statistical uncertainties.

Transmission electron microscopy (TEM) imaging was performed using a probe-corrected JEOL ARM 200F instrument operated at 200 kV. The cross-sectional TEM samples were prepared by FEI Helios Nanolab 600 or 600i dual-beam focused-ion beam FIB/SEM instruments following a standard lift-out procedure with a $SiO_2$ or C/Pt mask layer.

Sheet resistance of the films was determined as the slope of an $I-V$ curve measured by a four-point probe (FPP, Signatone SP4−40045TRS probe head connected to a Keithley 2400 SourceMeter). Film resistivity was calculated by multiplying the sheet resistance by the film thickness measured by SE. To extract carrier concentration and mobility, AC Hall effect measurements were performed in van der Pauw geometry on approximately 1 × 1 $cm^2$ samples using a Lakeshore 8404 HMS instrument.

**4.3. Electrocatalysis.** Electrochemical measurements were performed using a three-electrode setup controlled by an Autolab PGSTAT302N potentiostat (Metrohm) and a custom-made glass cell. Working electrodes were constructed by depositing 7 nm thick $MoS_2$ thin films on glassy carbon (GC) plates (2.2 × 2.2 × 0.3 $cm^2$, SIGRADUR G, HTW Hochtemperatur-Werkstoffe GmbH). Prior to deposition, the GC plates were polished by using an aqueous dispersion of 50 nm $Al_2O_3$ nanoparticles (BASi) applied to a velvet polishing pad (BASi) followed by rinsing with deionized water. The polishing procedure results in $R_q \approx 1-3$ nm, which is similar to that of $MoS_2$ films. No signs of plasma damage or etching of the GC were observed after deposition.

The $MoS_2$/GC samples were mounted to a custom-made poly(ether ether ketone) (PEEK) sample holder exposing a 3.14 $cm^2$ area of the sample. The holder was connected to a rotating disk electrode (RDE) assembly. A graphite rod counter electrode (diameter 6.3 mm, 99%, metal basis, Thermo Scientific) was positioned in a separate compartment separated by a glass frit. A commercial saturated calomel electrode (SCE, CH instruments) reference electrode was located in another glass-frit separated compartment. A Luggin capillary was used to position the reference electrode close (~0.5 cm) to the working electrode.

Prior to use in the catalytic measurements, the SCE was externally referenced to ferrocenecarboxylic acid in 0.2 M phosphate buffer titrated with NaOH to pH 7 (284 mV vs SCE).[70] The reference potential determined by this method was then used to convert the measured potentials to a reversible hydrogen electrode (RHE) scale.

The cell was filled with ~100 mL of 0.5 M $H_2SO_4$ electrolyte (pH 0.3) prepared from concentrated $H_2SO_4$ (Fischer Chemical Optima) and ultrapure water (resistivity 18.2 MΩcm). The electrolyte was purged by bubbling $N_2$ for at least 30 min prior to measurements. During measurements, the gas flow was switched to purge the headspace above the electrolyte.

Measurement procedure began with an electrochemical impedance spectroscopy (EIS) measurement (−0.2 V vs SCE, 10 Hz to 100 kHz, 10 mV root-mean-square AC amplitude). The impedance of the data point with phase closest to 0 (typically at 50−100 kHz) was taken as the uncompensated resistance (typically 0.3−0.4 Ω) and was used for 100% $iR$ postmeasurement compensation of the measured CVs. Then, a set of CV scans were performed in an inert potential window (−0.2 to 0.4 V vs SCE) to estimate the initial double layer capacitance ($C_{dl}$). In these measurements, the scan rate was increased from 50 to 250 mV/s in 50 mV/s increments with three scans recorded per scan rate. Next, five cyclic voltammetry (CV) scans in the HER region (−0.2 to −0.9 V and back vs SCE) were recorded at a scan rate of 10 mV/s while the electrode was rotated at 1600 rpm. The data from the fifth scan were used to extract the overpotentials and Tafel slopes (reported after $iR$ compensation). Following these scans, the rotation was stopped, and visible bubbles (if any) physically removed with a glass pipet, followed by a second set of CV scans in inert region (identical to above) to estimate $C_{dl}$. This latter set of scans was used for determining the presented $C_{dl}$ values, as these were taken to better correspond to the sample state during HER compared to the measurements performed before HER. $C_{dl}$ was determined as the slope of the line fit to current densities of anodic scans at 0.4 V vs RHE at different scan rates.

## ■ ASSOCIATED CONTENT

### Supporting Information

The Supporting Information is available free of charge at https://pubs.acs.org/doi/10.1021/acsami.3c02466.

Schematic of the optimized PEALD cycles, demonstration of thickness control and uniformity; optimization and additional characterization (AFM, FPP, Raman, SE, SEM, TEM, XPS, XRD) of the ABC processes discussed in the article (A $B_{0.20}$ $C_{H2}$, $n$(A $B_{0.20}$) $C_{H2}$, and A $B_{0.20}$ $C_{Ar}$) as well as other tested processes (A $B_{0.20}$ $C_{H2/Ar}$, A $B_{0.80}$ $C_{H2S/Ar}$, A $B_{0.80}$ $C_{H2}$, and A $B_{0.80}$ $C_{Ar}$); discussion on substrate biasing and effect of ions on film growth; additional process and literature comparison, electrical characterization, and electrocatalysis data and discussion (PDF)

## ■ AUTHOR INFORMATION


### Corresponding Author

**Ageeth A. Bol** − *Department of Applied Physics and Science Education, Eindhoven University of Technology, Eindhoven 5600 MB, The Netherlands; Department of Chemistry, University of Michigan, Ann Arbor, Michigan 48109-1055, United States;* orcid.org/0000-0002-1259-6265; Email: a.a.bol@tue.nl

### Authors

**Miika Mattinen** − *Department of Applied Physics and Science Education, Eindhoven University of Technology, Eindhoven 5600 MB, The Netherlands;* Present Address: Department of Chemistry, University of Helsinki, PO Box 55, Helsinki 00014, Finland; orcid.org/0000-0003-4837-1823

**Jeff J. P. M. Schulpen** − *Department of Applied Physics and Science Education, Eindhoven University of Technology, Eindhoven 5600 MB, The Netherlands*

**Rebecca A. Dawley** − *Department of Chemistry, University of Michigan, Ann Arbor, Michigan 48109-1055, United States;* orcid.org/0009-0005-4284-5161

**Farzan Gity** − *Tyndall National Institute, University College Cork, Cork T12 R5CP, Ireland;* orcid.org/0000-0003-3128-1426

**Marcel A. Verheijen** − *Department of Applied Physics and Science Education, Eindhoven University of Technology, Eindhoven 5600 MB, The Netherlands; Eurofins Materials*

*Science Netherlands, Eindhoven 5656 AE, The Netherlands;* orcid.org/0000-0002-8749-7755

**Wilhelmus M. M. Kessels** − *Department of Applied Physics and Science Education, Eindhoven University of Technology, Eindhoven 5600 MB, The Netherlands;* orcid.org/0000-0002-7630-8226

Complete contact information is available at: https://pubs.acs.org/10.1021/acsami.3c02466

### Notes

The authors declare no competing financial interest.

## ■ ACKNOWLEDGMENTS

The work has received funding from The Netherlands Organization for Scientific Research (NWO) through Vici project 17846 "Defects, a curse or a blessing: tailoring defects in two-dimensional transition metal dichalcogenides by atomic layer deposition". F.G. acknowledges support of Science Foundation Ireland through the AMBER 2 project (12/RC/2278_P2). The TEM facility used in this work has received funding from Solliance and the Dutch province of Noord-Brabant. The authors gratefully acknowledge B. Krishnamoorthy, C. A. A. van Helvoirt, C. O. van Bommel, and J. J. A. Zeebregts (TU/e) for technical assistance and support. Dr. B. Barcones (TU/e) is acknowledged for FIB preparation of the TEM samples. Silke Peeters (TU/e) is thanked for performing XRD measurements. Dr. Harm Knoops (TU/e, Oxford Instruments) is acknowledged for insightful discussions and suggestions. We acknowledge Yi Shi (Oxford Instruments) for SE uniformity mapping and Wim-Arnold Bok (Detect 99 B.V.) for RBS and ERD measurements. Dr. Wei Chen and Prof. Emiel Hensen from Inorganic Materials & Catalysis (IMC) group at TU/e are acknowledged for discussions on HER setup. The authors also acknowledge Roy Wentz from the University of Michigan glass shop for custom glassblowing services. Finally, we thank The University of Michigan LSA Scientific Instrument Shop for assistance with design and creation of the sample holder used in electrochemical measurements.

## ■ REFERENCES

(1) Wilson, J. A.; Yoffe, A. D. The Transition Metal Dichalcogenides Discussion and Interpretation of the Observed Optical, Electrical and Structural Properties. *Adv. Phys.* **1969**, *18*, 193−335.

(2) Zhou, J.; Lin, J.; Huang, X.; Zhou, Y.; Chen, Y.; Xia, J.; Wang, H.; Xie, Y.; Yu, H.; Lei, J.; Wu, D.; Liu, F.; Fu, Q.; Zeng, Q.; Hsu, C.-H.; Yang, C.; Lu, L.; Yu, T.; Shen, Z.; Lin, H.; Yakobson, B. I.; Liu, Q.; Suenaga, K.; Liu, G.; Liu, Z. A Library of Atomically Thin Metal Chalcogenides. *Nature* **2018**, *556*, 355−359.

(3) Manzeli, S.; Ovchinnikov, D.; Pasquier, D.; Yazyev, O. V.; Kis, A. 2D Transition Metal Dichalcogenides. *Nat. Rev. Mater.* **2017**, *2*, 17033.

(4) Chhowalla, M.; Shin, H. S.; Eda, G.; Li, L.-J.; Loh, K. P.; Zhang, H. The Chemistry of Two-Dimensional Layered Transition Metal Dichalcogenide Nanosheets. *Nat. Chem.* **2013**, *5*, 263−275.

(5) Samadi, M.; Sarikhani, N.; Zirak, M.; Zhang, H.; Zhang, H.-L.; Moshfegh, A. Z. Group 6 Transition Metal Dichalcogenide Nanomaterials: Synthesis, Applications and Future Perspectives. *Nanoscale Horizons* **2018**, *3*, 90−204.

(6) Radisavljevic, B.; Radenovic, A.; Brivio, J.; Giacometti, V.; Kis, A. Single-Layer $MoS_2$ Transistors. *Nat. Nanotechnol.* **2011**, *6*, 147−150.

(7) Liu, Y.; Duan, X.; Shin, H. J.; Park, S.; Huang, Y.; Duan, X. Promises and Prospects of Two-Dimensional Transistors. *Nature* **2021**, *591*, 43−53.

(8) Lopez-Sanchez, O.; Lembke, D.; Kayci, M.; Radenovic, A.; Kis, A. Ultrasensitive Photodetectors Based on Monolayer $MoS_2$. *Nat. Nanotechnol.* **2013**, *8*, 497−501.

(9) Sarkar, D.; Xie, X.; Liu, W.; Cao, W.; Kang, J.; Gong, Y.; Kraemer, S.; Ajayan, P. M.; Banerjee, K. A Subthermionic Tunnel Field-Effect Transistor with an Atomically Thin Channel. *Nature* **2015**, *526*, 91−95.

(10) Jiang, D.; Liu, Z.; Xiao, Z.; Qian, Z.; Sun, Y.; Zeng, Z.; Wang, R. Flexible Electronics Based on 2D Transition Metal Dichalcogenides. *J. Mater. Chem. A* **2021**, *10*, 89−121.

(11) Corzo, D.; Tostado-Blázquez, G.; Baran, D. Flexible Electronics: Status, Challenges and Opportunities. *Front. Electron.* **2020**, *1*, 594003.

(12) Jaramillo, T. F.; Jørgensen, K. P.; Bonde, J.; Nielsen, J. H.; Horch, S.; Chorkendorff, I. Identification of Active Edge Sites for Electrochemical $H_2$ Evolution from $MoS_2$ Nanocatalysts. *Science* **2007**, *317*, 100−102.

(13) Li, R.; Liang, J.; Li, T.; Yue, L.; Liu, Q.; Luo, Y.; Hamdy, M. S.; Sun, Y.; Sun, X. Recent Advances in $MoS_2$-Based Materials for Electrocatalysis. *Chem. Commun.* **2022**, *58*, 2259−2278.

(14) Fu, Q.; Han, J.; Wang, X.; Xu, P.; Yao, T.; Zhong, J.; Zhong, W.; Liu, S.; Gao, T.; Zhang, Z.; Xu, L.; Song, B. 2D Transition Metal Dichalcogenides: Design, Modulation, and Challenges in Electrocatalysis. *Adv. Mater.* **2021**, *33*, 1907818.

(15) Cao, Y. Roadmap and Direction toward High-Performance $MoS_2$ Hydrogen Evolution Catalysts. *ACS Nano* **2021**, *15*, 11014−11039.

(16) Vesborg, P. C. K.; Seger, B.; Chorkendorff, I. Recent Development in Hydrogen Evolution Reaction Catalysts and Their Practical Implementation. *J. Phys. Chem. Lett.* **2015**, *6*, 951−957.

(17) Nazir, H.; Muthuswamy, N.; Louis, C.; Jose, S.; Prakash, J.; Buan, M. E. M.; Flox, C.; Chavan, S.; Shi, X.; Kauranen, P.; et al. Is the $H_2$ Economy Realizable in the Foreseeable Future? Part III: H2 Usage Technologies, Applications, and Challenges and Opportunities. *Int. J. Hydrogen Energy* **2020**, *45*, 28217−28239.

(18) Briggs, N.; Subramanian, S.; Lin, Z.; Li, X.; Zhang, X.; Zhang, K.; Xiao, K.; Geohegan, D.; Wallace, R.; Chen, L.-Q.; Terrones, M.; Ebrahimi, A.; Das, S.; Redwing, J.; Hinkle, C.; Momeni, K.; van Duin, A.; Crespi, V.; Kar, S.; Robinson, J. A. A Roadmap for Electronic Grade 2D Materials. *2D Mater.* **2019**, *6*, No. 022001.

(19) Novoselov, K. S.; Jiang, D.; Schedin, F.; Booth, T. J.; Khotkevich, V. V.; Morozov, S. V.; Geim, A. K. Two-Dimensional Atomic Crystals. *Proc. Natl. Acad. Sci. U. S. A.* **2005**, *102*, 10451−10453.

(20) Lee, Y.-H.; Zhang, X.-Q.; Zhang, W.; Chang, M.-T.; Lin, C.-T.; Chang, K.-D.; Yu, Y.-C.; Wang, J. T.-W.; Chang, C.-S.; Li, L.-J.; Lin, T.-W. Synthesis of Large-Area $MoS_2$ Atomic Layers with Chemical Vapor Deposition. *Adv. Mater.* **2012**, *24*, 2320−2325.

(21) Zhan, Y.; Liu, Z.; Najmaei, S.; Ajayan, P. M.; Lou, J. Large-Area Vapor-Phase Growth and Characterization of $MoS_2$ Atomic Layers on a $SiO_2$ Substrate. *Small* **2012**, *8*, 966−971.

(22) Cai, Z.; Liu, B.; Zou, X.; Cheng, H.-M. Chemical Vapor Deposition Growth and Applications of Two-Dimensional Materials and Their Heterostructures. *Chem. Rev.* **2018**, *118*, 6091−6133.

(23) Kang, K.; Xie, S.; Huang, L.; Han, Y.; Huang, P. Y.; Mak, K. F.; Kim, C.-J.; Muller, D.; Park, J. High-Mobility Three-Atom-Thick Semiconducting Films with Wafer-Scale Homogeneity. *Nature* **2015**, *520*, 656−660.

(24) Kim, T.; Mun, J.; Park, H.; Joung, D.; Diware, M.; Won, C.; Park, J.; Jeong, S.-H.; Kang, S.-W. Wafer-Scale Production of Highly Uniform Two-Dimensional $MoS_2$ by Metal-Organic Chemical Vapor Deposition. *Nanotechnology* **2017**, *28*, 18LT01.

(25) Jin, G.; Lee, C.-S.; Okello, O. F. N.; Lee, S.-H.; Park, M. Y.; Cha, S.; Seo, S.; Moon, G.; Min, S. Y.; Yang, D.-H.; Han, C.; Ahn, H.; Lee, J.; Choi, H.; Kim, J.; Choi, S.; Jo, M. Heteroepitaxial van der Waals Semiconductor Superlattices. *Nat. Nanotechnol.* **2021**, *16*, 1092−1098.

(26) Kim, Y.; Kang, S. K.; Oh, N. C.; Lee, H. D.; Lee, S. M.; Park, J.; Kim, H. Improved Sensitivity in Schottky Contacted Two-Dimen-

sional $MoS_2$ Gas Sensor. *ACS Appl. Mater. Interfaces* **2019**, *11*, 38902−38909.
(27) Zhao, Y.; Song, J. G.; Ryu, G. H.; Ko, K. Y.; Woo, W. J.; Kim, Y.; Kim, D.; Lim, J. H.; Lee, S.; Lee, Z.; Park, J.; Kim, H. Low-Temperature Synthesis of 2D $MoS_2$ on a Plastic Substrate for a Flexible Gas Sensor. *Nanoscale* **2018**, *10*, 9338−9345.
(28) Fenouillet-Beranger, C.; Brunet, L.; Batude, P.; Brevard, L.; Garros, X.; Cassé, M.; Lacord, J.; Sklenard, B.; Acosta-Alba, P.; Kerdilès, S.; Tavernier, A.; Vizioz, C.; Besson, P.; Gassilloud, R.; Pedini, J.-M.; Kanyandekwe, J.; Mazen, F.; Magalhaes-Lucas, A.; Cavalcante, C.; Bosch, D.; Ribotta, M.; Lapras, V.; Vinet, M.; Andrieu, F.; Arcamone, J. A Review of Low Temperature Process Modules Leading Up to the First (≲500 °C) Planar FDSOI CMOS Devices for 3-D Sequential Integration. *IEEE Trans. Electron Devices* **2021**, *68*, 3142−3148.
(29) George, S. M. Atomic Layer Deposition: An Overview. *Chem. Rev.* **2010**, *110*, 111−131.
(30) Johnson, R. W.; Hultqvist, A.; Bent, S. F. A Brief Review of Atomic Layer Deposition: From Fundamentals to Applications. *Mater. Today* **2014**, *17*, 236−246.
(31) Mattinen, M.; Leskelä, M.; Ritala, M. Atomic Layer Deposition of 2D Metal Dichalcogenides for Electronics, Catalysis, Energy Storage, and Beyond. *Adv. Mater. Interfaces* **2021**, *8*, 2001677.
(32) Kim, Y.; Woo, W. J.; Kim, D.; Lee, S.; Chung, S.; Park, J.; Kim, H. Atomic-Layer-Deposition-Based 2D Transition Metal Chalcogenides: Synthesis, Modulation, and Applications. *Adv. Mater.* **2021**, *33*, 2005907.
(33) Knoops, H. C. M.; Faraz, T.; Arts, K.; Kessels, W. M. M. E. Status and Prospects of Plasma-Assisted Atomic Layer Deposition. *J. Vac. Sci. Technol. A* **2019**, *37*, No. 030902.
(34) Profijt, H. B.; Potts, S. E.; van de Sanden, M. C. M.; Kessels, W. M. M. Plasma-Assisted Atomic Layer Deposition: Basics, Opportunities, and Challenges. *J. Vac. Sci. Technol. A* **2011**, *29*, No. 050801.
(35) Boris, D. R.; Wheeler, V. D.; Nepal, N.; Qadri, S. B.; Walton, S. G.; Eddy, C. R. The Role of Plasma in Plasma-Enhanced Atomic Layer Deposition of Crystalline Films. *J. Vac. Sci. Technol. A* **2020**, *38*, No. 040801.
(36) Sharma, A.; Verheijen, M. A.; Wu, L.; Karwal, S.; Vandalon, V.; Knoops, H. C. M.; Sundaram, R. S.; Hofmann, J. P.; Kessels, W. M. M.; Bol, A. A. Low-Temperature Plasma-Enhanced Atomic Layer Deposition of 2-D $MoS_2$: Large Area, Thickness Control and Tuneable Morphology. *Nanoscale* **2018**, *10*, 8615−8627.
(37) Balasubramanyam, S.; Shirazi, M.; Bloodgood, M. A.; Wu, L.; Verheijen, M. A.; Vandalon, V.; Kessels, W. M. M.; Hofmann, J. P.; Bol, A. A. Edge-Site Nano-Engineering of $WS_2$ by Low Temperature Plasma-Enhanced Atomic Layer Deposition for Electrocatalytic Hydrogen Evolution. *Chem. Mater.* **2019**, *31*, 5104−5115.
(38) Basuvalingam, S. B.; Zhang, Y.; Bloodgood, M. A.; Godiksen, R. H.; Curto, A. G.; Hofmann, J. P.; Verheijen, M. A.; Kessels, W. M. M.; Bol, A. A. Low Temperature Phase-Controlled Synthesis of Titanium Di- and Tri-Sulfide by Atomic Layer Deposition. *Chem. Mater.* **2019**, *31*, 9354−9362.
(39) Mattinen, M.; Gity, F.; Coleman, E.; Vonk, J. F. A.; Verheijen, M. A.; Duffy, R.; Kessels, W. M. M.; Bol, A. A. Atomic Layer Deposition of Large-Area Polycrystalline Transition Metal Dichalcogenides from 100 °C through Control of Plasma Chemistry. *Chem. Mater.* **2022**, *34*, 7280−7292.
(40) Gudmundsson, J. T. Ion Energy Distribution in $H_2$/Ar Plasma in a Planar Inductive Discharge. *Plasma Sources Sci. Technol.* **1999**, *8*, 58−64.
(41) Arts, K.; Thepass, H.; Verheijen, M. A.; Puurunen, R. L.; Kessels, W. M. M.; Knoops, H. C. M. Impact of Ions on Film Conformality and Crystallinity during Plasma-Assisted Atomic Layer Deposition of $TiO_2$. *Chem. Mater.* **2021**, *33*, 5002−5009.
(42) Balasubramanyam, S.; Bloodgood, M. A.; van Ommeren, M.; Faraz, T.; Vandalon, V.; Kessels, W. M. M.; Verheijen, M. A.; Bol, A. A. Probing the Origin and Suppression of Vertically Oriented Nanostructures of 2D $WS_2$ Layers. *ACS Appl. Mater. Interfaces* **2020**, *12*, 3873−3885.
(43) Langereis, E.; Heil, S. B. S.; Knoops, H. C. M.; Keuning, W.; van de Sanden, M. C. M.; Kessels, W. M. M. In Situ Spectroscopic Ellipsometry as a Versatile Tool for Studying Atomic Layer Deposition. *J. Phys. D. Appl. Phys.* **2009**, *42*, No. 073001.
(44) Faraz, T.; Arts, K.; Karwal, S.; Knoops, H. C. M.; Kessels, W. M. M. Energetic Ions during Plasma-Enhanced Atomic Layer Deposition and Their Role in Tailoring Material Properties. *Plasma Sources Sci. Technol.* **2019**, *28*, No. 024002.
(45) Faraz, T.; Verstappen, Y. G. P.; Verheijen, M. A.; Chittock, N. J.; Lopez, J. E.; Heijdra, E.; Van Gennip, W. J. H.; Kessels, W. M. M.; Mackus, A. J. M. Precise Ion Energy Control with Tailored Waveform Biasing for Atomic Scale Processing. *J. Appl. Phys.* **2020**, *128*, 213301.
(46) Profijt, H. B.; Kessels, W. M. M. Ion Bombardment during Plasma-Assisted Atomic Layer Deposition. *ECS Trans.* **2013**, *50* (13), 23−34.
(47) Profijt, H. B.; van de Sanden, M. C. M.; Kessels, W. M. M. Substrate-Biasing during Plasma-Assisted Atomic Layer Deposition to Tailor Metal-Oxide Thin Film Growth. *J. Vac. Sci. Technol. A* **2013**, *31*, No. 01A106.
(48) Faraz, T.; Knoops, H. C. M.; Verheijen, M. A.; Van Helvoirt, C. A. A.; Karwal, S.; Sharma, A.; Beladiya, V.; Szeghalmi, A.; Hausmann, D. M.; Henri, J.; Creatore, M.; Kessels, W. M. M. Tuning Material Properties of Oxides and Nitrides by Substrate Biasing during Plasma-Enhanced Atomic Layer Deposition on Planar and 3D Substrate Topographies. *ACS Appl. Mater. Interfaces* **2018**, *10*, 13158−13180.
(49) Lin, T.; Kang, B.; Jeon, M.; Huffman, C.; Jeon, J.; Lee, S.; Han, W.; Lee, J.; Lee, S.; Yeom, G.; Kim, K. Controlled Layer-by-Layer Etching of $MoS_2$. *ACS Appl. Mater. Interfaces* **2015**, *7*, 15892−15987.
(50) Lu, W.; Birmingham, B.; Zhang, Z. Defect Engineering on $MoS_2$ Surface with Argon Ion Bombardments and Thermal Annealing. *Appl. Surf. Sci.* **2020**, *532*, 147461.
(51) Ghorbani-Asl, M.; Kretschmer, S.; Spearot, D. E.; Krasheninnikov, A. V. Two-Dimensional $MoS_2$ under Ion Irradiation: From Controlled Defect Production to Electronic Structure Engineering. *2D Mater.* **2017**, *4*, No. 025078.
(52) Kretschmer, S.; Maslov, M.; Ghaderzadeh, S.; Ghorbani-Asl, M.; Hlawacek, G.; Krasheninnikov, A. V. Supported Two-Dimensional Materials under Ion Irradiation: The Substrate Governs Defect Production. *ACS Appl. Mater. Interfaces* **2018**, *10*, 30827−30836.
(53) Knoops, H. C. M.; Arts, K.; Buiter, J. W.; Martini, L. M.; Engeln, R.; Hemakumara, D. T.; Powell, M.; Kessels, W. M. M.; Hodson, C. J.; O'Mahony, A. Innovative Remote Plasma Source for Atomic Layer Deposition for GaN Devices. *J. Vac. Sci. Technol. A* **2021**, *39*, No. 062403.
(54) Mignuzzi, S.; Pollard, A. J.; Bonini, N.; Brennan, B.; Gilmore, I. S.; Pimenta, M. A.; Richards, D.; Roy, D. Effect of Disorder on Raman Scattering of Single-Layer $MoS_2$. *Phys. Rev. B* **2015**, *91*, 195411.
(55) Mattinen, M.; Hatanpää, T.; Sarnet, T.; Mizohata, K.; Meinander, K.; King, P. J.; Khriachtchev, L.; Räisänen, J.; Ritala, M.; Leskelä, M. Atomic Layer Deposition of Crystalline $MoS_2$ Thin Films: New Molybdenum Precursor for Low-Temperature Film Growth. *Adv. Mater. Interfaces* **2017**, *4*, 1700123.
(56) Hämäläinen, J.; Mattinen, M.; Mizohata, K.; Meinander, K.; Vehkamäki, M.; Räisänen, J.; Ritala, M.; Leskelä, M. Atomic Layer Deposition of Rhenium Disulfide. *Adv. Mater.* **2018**, *30*, 1703622.
(57) Ganta, D.; Sinha, S.; Haasch, R. T. 2-D Material Molybdenum Disulfide Analyzed by XPS. *Surf. Sci. Spectra* **2014**, *21*, 19−27.
(58) Krbal, M.; Prokop, V.; Kononov, A. A.; Pereira, J. R.; Mistrik, J.; Kolobov, A. V.; Fons, P. J.; Saito, Y.; Hatayama, S.; Shuang, Y.; Sutou, Y.; Rozhkov, S. A.; Stellhorn, J. R.; Hayakawa, S.; Pis, I.; Bondino, F. Amorphous-to-Crystal Transition in Quasi-Two-Dimensional $MoS_2$: Implications for 2D Electronic Devices. *ACS Appl. Nano Mater.* **2021**, *4*, 8834−8844.
(59) Weber, T.; Muijsers, J. C.; Van Wolput, J. H. M. C.; Verhagen, C. P. J.; Niemantsverdriet, J. W. Basic Reaction Steps in the Sulfidation of Crystalline $MoO_3$ to $MoS_2$, as Studied by X-Ray Photoelectron and Infrared Emission Spectroscopy. *J. Phys. Chem.* **1996**, *100*, 14144−14150.


https://doi.org/10.1021/acsami.3c02466
ACS Appl. Mater. Interfaces 2023, 15, 35565−35579

(60) *NIST X-ray Photoelectron Spectroscopy Database, Version 4.1*; National Institute of Standards and Technology: Gaithersburg, MD, 2012; http://srdata.nist.gov/xps/ (accessed July 2022).
(61) Weber, T.; Muijsers, J. C.; Niemantsverdriet, J. W. Structure of Amorphous $MoS_3$. *J. Phys. Chem.* **1995**, *99*, 9194−9200.
(62) Li, B.; Jiang, L.; Li, X.; Cheng, Z.; Ran, P.; Zuo, P.; Qu, L.; Zhang, J.; Lu, Y. Controllable Synthesis of Nanosized Amorphous $MoS_x$ Using Temporally Shaped Femtosecond Laser for Highly Efficient Electrochemical Hydrogen Production. *Adv. Funct. Mater.* **2019**, *29*, 1806229.
(63) Anantharaj, S.; Ede, S. R.; Karthick, K.; Sam Sankar, S.; Sangeetha, K.; Karthik, P. E.; Kundu, S. Precision and Correctness in the Evaluation of Electrocatalytic Water Splitting: Revisiting Activity Parameters with a Critical Assessment. *Energy Environ. Sci.* **2018**, *11*, 744−771.
(64) McCrory, C. C. L.; Jung, S.; Ferrer, I. M.; Chatman, S. M.; Peters, J. C.; Jaramillo, T. F. Benchmarking Hydrogen Evolving Reaction and Oxygen Evolving Reaction Electrocatalysts for Solar Water Splitting Devices. *J. Am. Chem. Soc.* **2015**, *137*, 4347−4357.
(65) Morales-Guio, C. G.; Hu, X. Amorphous Molybdenum Sulfides as Hydrogen Evolution Catalysts. *Acc. Chem. Res.* **2014**, *47*, 2671−2681.
(66) Benck, J. D.; Hellstern, T. R.; Kibsgaard, J.; Chakthranont, P.; Jaramillo, T. F. Catalyzing the Hydrogen Evolution Reaction (HER) with Molybdenum Sulfide Nanomaterials. *ACS Catal.* **2014**, *4*, 3957−3971.
(67) MacIsaac, C.; Schneider, J. R.; Closser, R. G.; Hellstern, T. R.; Bergsman, D. S.; Park, J.; Liu, Y.; Sinclair, R.; Bent, S. F. Atomic and Molecular Layer Deposition of Hybrid Mo-Thiolate Thin Films with Enhanced Catalytic Activity. *Adv. Funct. Mater.* **2018**, *28*, 1800852.
(68) Wiensch, J. D.; John, J.; Velazquez, J. M.; Torelli, D. A.; Pieterick, A. P.; McDowell, M. T.; Sun, K.; Zhao, X.; Brunschwig, B. S.; Lewis, N. S. Comparative Study in Acidic and Alkaline Media of the Effects of PH and Crystallinity on the Hydrogen-Evolution Reaction on $MoS_2$ and $MoSe_2$. *ACS Energy Lett.* **2017**, *2*, 2234−2238.
(69) Sun, T.; Zhang, G.; Xu, D.; Lian, X.; Li, H.; Chen, W.; Su, C. Defect chemistry in 2D materials for electrocatalysis. *Mater. Today Energy* **2019**, *12*, 215−238.
(70) Liaudet, E.; Battaglini, F.; Calvo, E. J. Electrochemical Study of Sulphonated Ferrocenes as Redox Mediators in Enzyme Electrodes. *J. Electroanal. Chem.* **1990**, *293*, 55−68.


https://doi.org/10.1021/acsami.3c02466
*ACS Appl. Mater. Interfaces* 2023, 15, 35565−35579